

Sensitivity of a Simulated Squall Line to Horizontal Resolution and Parameterization of Microphysics

GEORGE H. BRYAN AND HUGH MORRISON

National Center for Atmospheric Research, Boulder, Colorado*

(Manuscript received 25 February 2011, in final form 15 June 2011)

ABSTRACT

Idealized simulations of the 15 May 2009 squall line from the Second Verification of the Origins of Rotation in Tornadoes Experiment (VORTEX2) are evaluated in this study. Four different microphysical setups are used, with either single-moment (1M) or double-moment (2M) microphysics, and either hail or graupel as the dense (rimed) ice species. Three different horizontal grid spacings are used: $\Delta x = 4, 1$, or 0.25 km (with identical vertical grids). Overall, results show that simulated squall lines are sensitive to both microphysical setup and horizontal resolution, although some quantities (i.e., surface rainfall) are more sensitive to Δx in this study. Simulations with larger Δx are slower to develop, produce more precipitation, and have higher cloud tops, all of which are attributable to larger convective cells that do not entrain midlevel air. The highest-resolution simulations have substantially more cloud water evaporation, which is partly attributable to the development of *resolved* turbulence. For a given Δx , the 1M simulations produce less rain, more intense cold pools, and do not have trailing stratiform precipitation at the surface, owing to excessive rainwater evaporation. The simulations with graupel as the dense ice species have unrealistically wide convective regions. Comparison against analyses from VORTEX2 data shows that the 2M setup with hail and $\Delta x = 0.25$ km produces the most realistic simulation because (i) this simulation produces realistic distributions of reflectivity associated with convective, transition, and trailing stratiform regions, (ii) the cold pool properties are reasonably close to analyses from VORTEX2, and (iii) relative humidity in the cold pool is closest to observations.

1. Introduction

Organized systems of deep convection (mesoscale convective systems) are a key component of weather in the tropics and midlatitudes, producing a large proportion of the earth's precipitation (e.g., Houze 1993). Cloud-system-resolving models (CSRMs) using horizontal grid spacing of $O(1)$ km are naturally suited to study these systems because they can explicitly resolve the mesoscale and larger convective-scale dynamics. Thus, with recent advances in computing power they have been used for regional-scale numerical weather prediction (NWP), with a focus on warm season convection forecasting (e.g., Done et al. 2004; Kain et al. 2008; Weisman et al. 2008).

Many operational forecast centers are now using, or soon plan to use, horizontal grid spacing of $O(1)$ km (e.g., Weiss et al. 2008; Lean et al. 2008; Seity et al. 2011; Baldauf et al. 2011). Furthermore, CSRMs are now being utilized as higher-resolution models embedded within coarser-resolution general circulation models [i.e., the multiscale modeling framework or "superparameterization" (e.g., Grabowski 2001; Randall et al. 2003)].

Despite the inherent ability of CSRMs to better resolve the dynamics of mesoscale convective systems relative to larger-scale models, there are limitations and uncertainties, especially with regard to the physical processes occurring on subgrid scales. These processes include cloud and precipitation microphysics, cloud-radiative interaction, exchange with the surface, and subgrid-scale turbulence. Furthermore, the coupling between these processes, and how these processes and their interactions both respond to and drive the cloud-scale and mesoscale dynamics, are important research topics. It seems likely that differences in the parameterization of these subgrid components, and hence their interactions with the resolved flow, are responsible in part for differences among

* The National Center for Atmospheric Research is sponsored by the National Science Foundation.

Corresponding author address: George H. Bryan, National Center for Atmospheric Research, 3090 Center Green Drive, Boulder, CO 80301.
E-mail: gbryan@ucar.edu

CSRM simulations in model intercomparison studies of deep convection (e.g., Xu et al. 2002; Redelsperger et al. 2000; Bryan et al. 2006; Grabowski et al. 2006).

An important aspect of the interaction between the parameterized subgrid model components and the resolved-scale dynamics is the model grid spacing. Horizontal grid spacing of $O(1\text{ km})$ is often considered sufficient to simulate deep moist convection, based on the argument that nonhydrostatic processes can be represented at this resolution (Weisman et al. 1997). Thus, the implicit assumption is that traditional subgrid-scale turbulence parameterizations can properly account for the intra-cloud motions and turbulent eddies in deep convective clouds. However, several studies have documented the sensitivity of deep convection simulations to horizontal grid spacing at scales below 1 km (e.g., Grabowski 1998; Adlerman and Droegemeier 2002; Petch and Gray 2001; Petch et al. 2002; Bryan et al. 2003; Rotunno et al. 2009; Dawson et al. 2010). Bryan et al. (2003) showed that grid spacing of 250 m or less was needed to resolve an inertial subrange, and thus be consistent with the design of traditional turbulence closures used by CSRMs that follow techniques developed for large-eddy simulation (LES). They found that while overall storm characteristics were qualitatively similar, there were differences in precipitation amount, system phase speed, cloud depth, and organizational mode between simulations using horizontal grid spacing of $O(1\text{ km})$ and $O(100\text{ m})$.

The parameterization of microphysics also represents an important source of uncertainty in CSRM simulations of organized deep convection. Microphysics directly impacts buoyancy and hence convective fluxes through condensate loading and latent heating/cooling. Some early CSRM simulations of deep convection used liquid-only microphysics schemes (e.g., Weisman et al. 1988; LaFore and Moncrieff 1989). However, some studies have illustrated the clear importance of ice microphysics on system structure and intensity (e.g., Lord et al. 1984; Fovell and Ogura 1988; Liu et al. 1997; Gilmore et al. 2004a). Ice microphysics impacts organized convection primarily via the extra latent heating due to freezing and the latent cooling due to melting, as well as the generally slower fall speed of ice (and hence longer residence time in the atmosphere) compared to rain (Liu et al. 1997). However, numerous uncertainties with regard to microphysics schemes remain, especially for the ice phase.

One key uncertainty in parameterizing ice microphysics is the number and type of ice species (e.g., cloud ice, snow, graupel, hail, etc.) (Fovell and Ogura 1988; McCumber et al. 1991; Ferrier et al. 1995; Gilmore et al. 2004b; VanWeverberg et al. 2010; Morrison and Milbrandt 2011). Partitioning of ice into different species with fixed characteristics is done in most bulk microphysics schemes

to represent the wide range of ice particle types observed in the atmosphere. These characteristics, which include terminal fall-speed size and density–size relationships, vary widely among different ice categories in bulk schemes (Gilmore et al. 2004b; Straka and Mansell 2005; Morrison and Milbrandt 2011). The paradigm of including different classes of ice with fixed characteristics leads to uncertainty given that, in nature, ice particles exhibit a continuum of characteristics (cf. Morrison and Grabowski 2008). Thus, it seems likely that tuning schemes to produce realistic results in one case may lead to degraded results in other cases. Consistent with this argument, previous studies have shown a large sensitivity to the number and type of ice species. For example, Fovell and Ogura (1988) found that a three-class bulk scheme (cloud ice, snow, hail) improved the simulation of precipitation and radar reflectivity along the leading edge of a squall line relative to using a two-class scheme with only cloud ice and snow. McCumber et al. (1991) showed large sensitivity of a tropical squall-line simulation to inclusion of either graupel or hail in a three-class bulk scheme, and found that the scheme with graupel produced more realistic results.

Recent development of bulk microphysics parameterizations has also included the prediction of multiple moments of the hydrometeor size distributions (e.g., Koenig and Murray 1976; Ferrier 1994; Meyers et al. 1997; Cohard and Pinty 2000; Seifert and Beheng 2001; Milbrandt and Yau 2005a,b; Morrison et al. 2009; Phillips et al. 2007). Two-moment (2M) bulk schemes predict both the mixing ratios and number concentrations of the hydrometeor size distributions of various species, as opposed to one-moment (1M) schemes that predict mixing ratios only. The prediction of both mixing ratio and number concentration increases the degrees of freedom and allows for a more flexible treatment of the particle size distributions, although there is an increase in computational cost. We note that two-moment schemes have also been widely used to treat droplet activation and cloud–aerosol interaction via prediction of the droplet number concentration (e.g., Ghan et al. 1997; Cohard and Pinty 2000; Morrison et al. 2005, hereafter M05; Seifert and Beheng 2006a,b; Phillips et al. 2007; Ming et al. 2007). In terms of organized deep convection, key processes that are impacted by using two-moment versus one-moment schemes include particle size sorting and rain evaporation (Milbrandt and Yau 2005b; Morrison et al. 2009; Luo et al. 2010). Morrison et al. (2009) found that a two-moment scheme reduced rain evaporation in the trailing stratiform region of a squall line relative to a one-moment version of the same scheme, leading to increased stratiform precipitation at the surface, a weakened cold pool, and a more realistic

vertical profile of radar reflectivity. Similarly, weaker cold pools in supercell simulations produced by a two-moment scheme compared to a one-moment version of the same scheme led to improvement relative to observations (Milbrandt and Yau 2005b; Dawson et al. 2010). While these studies suggest there are important differences in results using one-moment versus two-moment schemes, little work has been done to compare this sensitivity to that arising from other important aspects of the microphysics, such as the number and type of ice species.

The key point is that uncertainties related to the parameterization of microphysics and model resolution may be closely linked, since microphysics schemes are largely driven by the resolved-scale motions. We hypothesize that good quantitative performance of $O(1\text{ km})$ models relative to observations (in terms of quantities such as radar reflectivity or surface precipitation rate) may sometimes result from compensating errors and implicit tunings of parameterizations, for example, microphysical parameter settings that compensate for the marginal grid spacing and the lack of explicit turbulent entrainment. The upshot is that as the complexity increases and realism of microphysics schemes improves, problems related to marginal grid spacing or other model deficiencies (radiation, boundary layer, surface parameterizations, etc.) may become exposed. Thus, it is important to concurrently examine sensitivities to model grid spacing and the parameterization of microphysics.

Herein we analyze idealized three-dimensional numerical simulations of a well-observed squall line from the Second Verification of the Origins of Rotation in Tornadoes Experiment (VORTEX2). The primary focus is on the sensitivity of the structure and intensity of the squall line (i.e., precipitation characteristics and amount, cloud depth, system phase speed, upward mass flux, cold pool strength, etc.) to horizontal grid spacing between 4 and 0.25 km, as well as two key aspects of a three-class bulk microphysics parameterization: 1) one moment versus two moment and 2) inclusion of either graupel or hail as the dense precipitating ice species. The paper is organized as follows: section 2 briefly describes the modeling framework; further details are also provided in the appendix. Results of the resolution sensitivity are described in section 3, and results of the sensitivity to microphysics parameterization are described in section 4. Comparison of the model output to VORTEX2 data is presented in section 5, and a summary is presented in section 6.

2. Methodology

a. Numerical model and setup

The three-dimensional nonhydrostatic numerical model Cloud Model version 1 (CM1) is used for the simulations.

Some technical details are provided in the appendix. The observed squall line was extraordinarily long (it extended from Texas to Illinois), so we simulate only a portion of the line with periodic lateral boundary conditions in the along-line (y) direction. Open boundary conditions are used in the longer across-line (x) direction. The domain size is $576\text{ km} \times 144\text{ km} \times 25\text{ km}$. Three different horizontal grid spacings (Δx) are used for this study: 4, 1, and 0.25 km. The vertical grid is the same for all simulations; there are 100 levels with vertical grid spacing increasing from 100 m at the surface to 400 m at the top of the domain. Such high vertical resolution is needed to produce three-dimensional turbulence in the $\Delta x = 0.25\text{-km}$ simulation and we hold the vertical resolution fixed for all simulations for consistency.

A time step of 3 s is used for all simulations. Radiative transfer, surface heat fluxes, and Coriolis acceleration are neglected for simplicity and to ensure that the environment remains the same for all simulations. A Rayleigh damper is used in the upper 6 km of the domain to dampen waves in the stratosphere. Surface drag is calculated on perturbation winds, such that the mean environmental wind shear is not affected, with a constant drag coefficient of 0.01. The squall line is initialized with a cold pool as in Weisman et al. (1997). Random temperature perturbations ($\pm 0.2\text{ K}$) are inserted near the edge of the cold pool to initiate three-dimensional motions.

For some analyses, we plot results in terms of distance normal to the surface gust front (x_c). The surface gust front is defined by the location of the -1-K perturbation potential temperature contour at the lowest model level. Line-averaged results are obtained by first converting the model output to an (x_c, y, z) coordinate, and then averaging in y .

b. Microphysics parameterization

1) TWO-MOMENT SCHEME

The two-moment bulk cloud microphysics scheme predicts mixing ratios and number concentrations of five hydrometeor species: cloud droplets, cloud ice, snow, rain, and either graupel or hail. This scheme is based on the parameterization of M05, and subsequently implemented, with modifications, into the fifth-generation Pennsylvania State University–National Center for Atmospheric Research Mesoscale Model (MM5; Morrison and Pinto 2005, 2006; Morrison et al. 2008) and the Weather Research and Forecasting model (WRF; Morrison et al. 2009). The hydrometeor size distributions $N(D)$ are treated using gamma functions:

$$N(D) = N_0 D^\mu e^{-\lambda D}, \quad (1)$$

where D is the particle diameter, and N_0 , μ , and λ are the intercept, shape, and slope parameters, respectively. For

TABLE 1. Specified constant values of size distribution intercept parameter N_0 for the precipitation species in the 1M scheme.

Species	N_0 (m^{-4})	Reference
Rain	10^7	Dudhia (1989), Grabowski (1998)*
Snow	2×10^7	Dudhia (1989)**
Graupel	4×10^6	Rutledge and Hobbs (1984), Reisner et al. (1998), Hong et al. (2004)

* Lin et al. (1983), Rutledge and Hobbs (1984), Reisner et al. (1998), and Hong et al. (2004) used a similar value of 8×10^6 .

** Grabowski (1998) used a similar value of 10^7 .

the precipitation species as well as cloud ice, we assume that $\mu = 0$ (i.e., an inverse exponential distribution). For cloud droplets, μ is a function of the predicted droplet number concentration following the observations of Martin et al. (1994). In the two-moment version of the scheme, N_0 and λ are free parameters that are determined from the predicted mixing ratio and number concentration for each species, as described in the appendix.

2) ONE-MOMENT SCHEME

The one-moment scheme is exactly the same as the two-moment scheme described above, except that the number concentrations of the precipitation species are diagnosed, not predicted. Thus, N_0 is specified for rain, snow, and graupel, and N and λ are derived from the predicted q and specified N_0 and μ for each species by rearranging terms in (A6) and (A7). Following many one-moment schemes (e.g., Lin et al. 1983; Rutledge and Hobbs 1984; Dudhia 1989; Grabowski 1998), N_0 is constant for a given species. Values are taken from existing schemes described in the literature and shown in Table 1. Note that while most one-moment schemes use constant values of N_0 , it is not an intrinsic feature of these schemes; some allow N_0 to vary for rain, snow, and/or graupel/hail as a function of the predicted cloud or thermodynamic variables (e.g., mixing ratio of the species, or air temperature). For example, Reisner et al. (1998) and Hong et al. (2004) allow variable N_0 for snow, while Thompson et al. (2004, 2008) allow variable N_0 for all precipitation species (snow, graupel, and rain).

3) HAIL AND GRAUPEL MICROPHYSICS

For 1M and 2M simulations, we test the impact of assuming either graupel or hail for the dense (rimed) ice species by setting the bulk particle density to either a lower value appropriate for medium-density graupel (400 kg m^{-3}) following Reisner et al. (1998) or high-density hail (900 kg m^{-3}) similar to Lin et al. (1983). Fall speed parameters are also modified to correspond to either graupel or hail. The fall speed–size relationship is

given by a power law, $V = aD^b$. For graupel, $a = 19.3 \text{ m}^{1-b} \text{ s}^{-1}$ and $b = 0.37$ following the relationship in Locatelli and Hobbs (1974) for lump graupel. For hail, $a = 114.5 \text{ m}^{1-b} \text{ s}^{-1}$ and $b = 0.5$ following Matson and Huggins (1980). These runs are referred to as either “HAIL” or “GRPL” (i.e., 1M-HAIL, 2M-HAIL, 1M-GRPL, 2M-GRPL). All other microphysical processes for hail are treated exactly the same as graupel (see Morrison et al. 2009), so that the only differences between the hail and graupel versions of the scheme are the particle density– and fall speed–size relationships as described above. While it is well-known that graupel and hail growth processes generally differ (e.g., wet growth leading to hail and dry growth to graupel) (e.g., Pruppacher and Klett 1997), varying only the density and fall speed relationships between the graupel and hail runs greatly simplifies the analysis and allows us to isolate causes of differences among these simulations to specific parameter choices.

c. Case description

For this study we are interested in midlatitude squall lines with trailing stratiform regions. To allow for some basic evaluation with observations, we initialize the model with the environment of the 15 May 2009 squall line that was observed during VORTEX2. A detailed description of this case was presented by Bryan and Parker (2010, hereafter BP10). A sounding launched at 2138 UTC in the prestorm environment ($\sim 100 \text{ km}$ ahead of the squall line) is used for the initial condition (Fig. 1). This sounding has large CAPE (4200 J kg^{-1}) and fairly weak deep-layer shear (line-normal wind speed difference of 10 m s^{-1} between 0.5 and 10 km AGL). This case is attractive for use in this study because of the eight additional rawinsondes that were launched as part of the VORTEX2 data collection. These data allow for a subjective evaluation of the thermodynamic and kinematic structure of the simulated squall lines, which is the focus of a later section of this article.

3. Sensitivity to horizontal resolution

We first look at the properties of individual convective cells. Horizontal cross sections of vertical velocity w (Fig. 2) clearly show that cell size is proportional to Δx over this range of Δx . In fact, the width of midlevel updrafts tends to be about 4–6 times the horizontal grid spacing for $\Delta x = 4$ and 1 km (Figs. 2a,b), whereas a broader spectrum of updraft sizes occurs with $\Delta x = 0.25 \text{ km}$ (Fig. 2c). These conclusions hold for all microphysical setups, so we show only the 2M-HAIL case in this figure. The interpretation here is straightforward: the $\Delta x = 4\text{-km}$ simulation is simply forced to represent convection on the smallest resolvable scale, whereas the $\Delta x = 0.25\text{-km}$

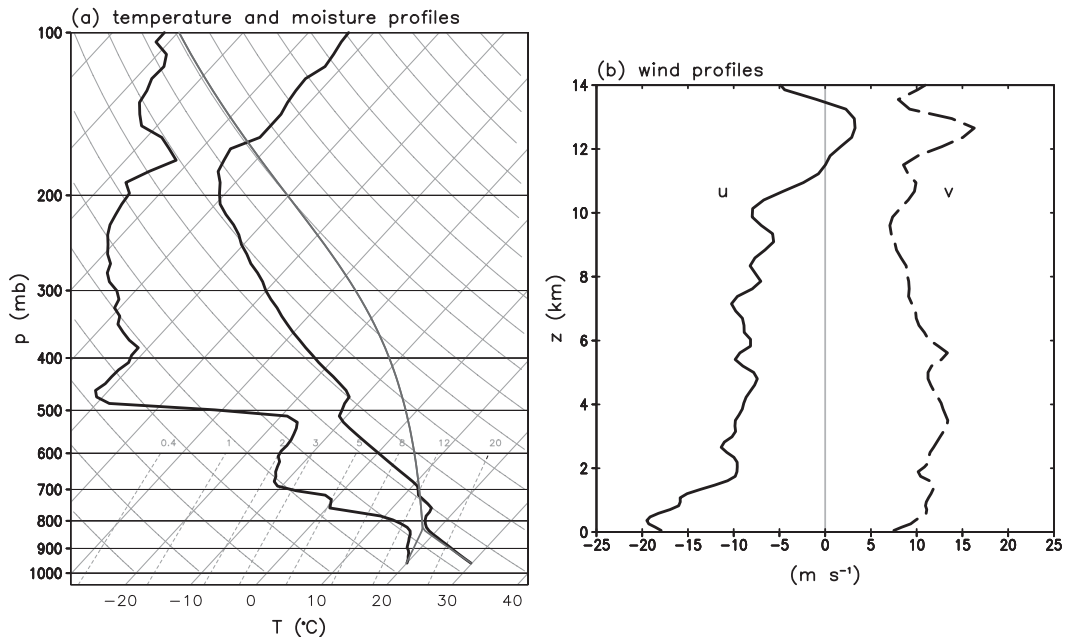


FIG. 1. Initial profiles of (a) temperature and moisture and (b) system-relative along-line winds (u) and across-line winds (v).

simulations can develop a broader spectrum of convective motions, as discussed by Bryan et al. (2003).

To illustrate one of the more notable impacts of different cell size, we show the cloud water evaporation rate (E_c) as contours in Fig. 2. This microphysical process tends to occur primarily in two places: 1) on the edges of clouds and 2) in downdrafts. Because clouds are smaller and more numerous with smaller Δx , there is a much greater surface area for evaporation to occur. To provide

another perspective, we show vertical cross sections in Fig. 3, where Figs. 3a–c show along-line cross sections through a convective cell, and Figs. 3d–f show across-line cross sections through the same cell. These views reinforce the conclusions that more cells exist and E_c is more prevalent as Δx decreases.

It is unclear whether changes in domain-total E_c (shown later) are entirely attributable to the greater number and surface area of convective clouds, or whether numerical

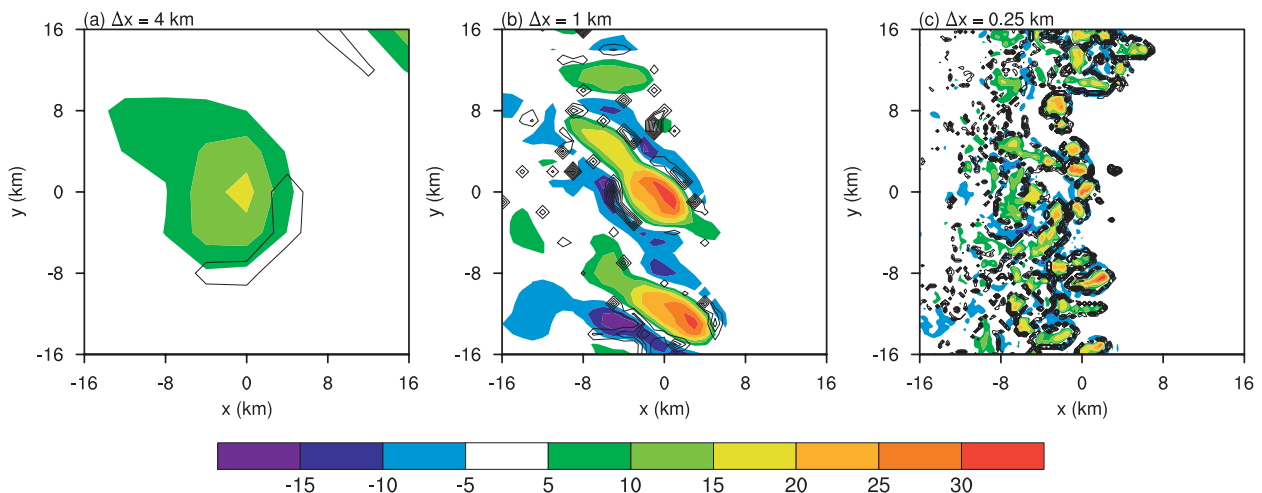


FIG. 2. Horizontal cross sections (over a $32 \text{ km} \times 32 \text{ km}$ subdomain) at $z = 5$ km and $t = 6$ h for 2M-HAIL using (a) $\Delta x = 4$ km, (b) $\Delta x = 1$ km, and (c) $\Delta x = 0.25$ km. Shading is vertical velocity w (m s^{-1}) and contours are cloud water evaporation rate E_c (contour interval is $1 \times 10^5 \text{ kg kg}^{-1} \text{ s}^{-1}$).

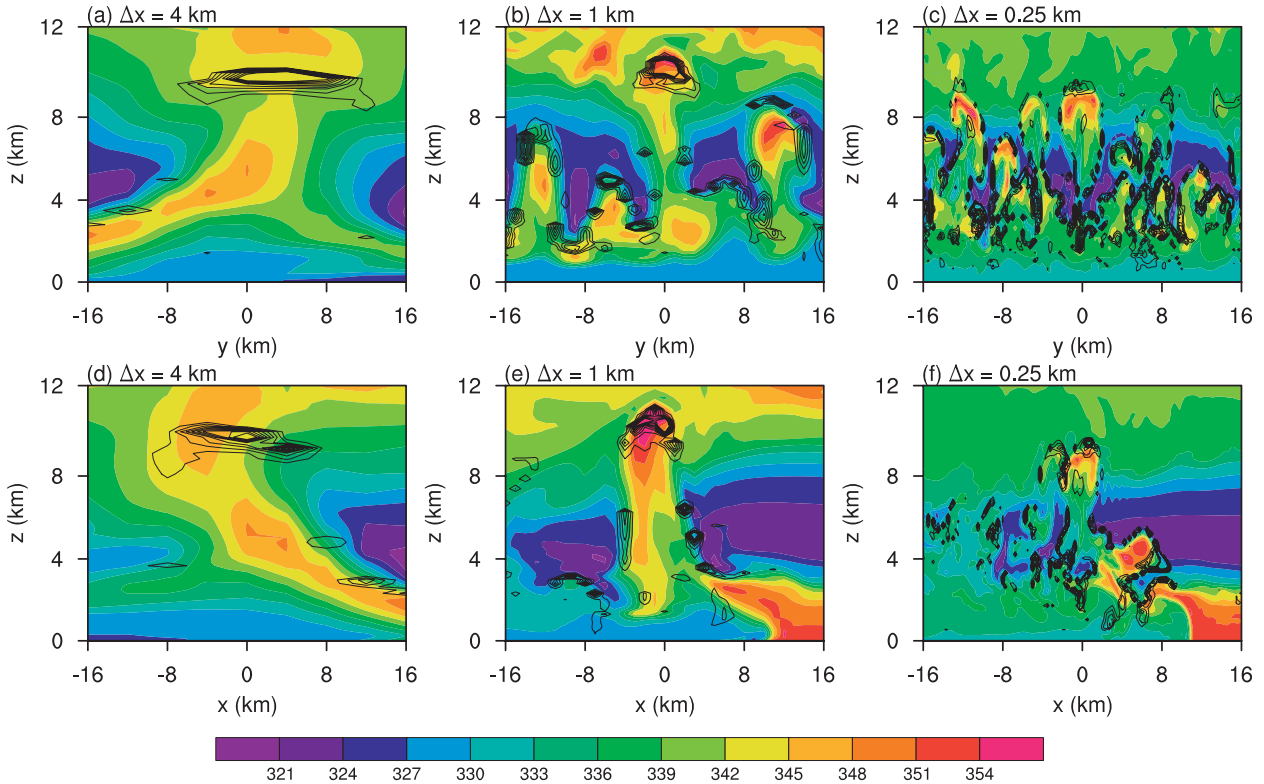


FIG. 3. Vertical cross sections (a)–(c) along the line and (d)–(f) across the line for the (a),(d) $\Delta x = 4\text{-km}$ simulation, (b),(e) $\Delta x = 1\text{-km}$ simulation, and (c),(f) $\Delta x = 0.25\text{-km}$ simulation for the same simulations at the same time as Fig. 2. Shading is equivalent potential temperature θ_e (K) and contours are cloud water evaporation rate E_c (contour interval is $1 \times 10^5 \text{ kg kg}^{-1} \text{ s}^{-1}$).

issues play a significant role. The well-known “advection–condensation problem” (e.g., Grabowski and Smolarkiewicz 1990; Stevens et al. 1996; Grabowski and Morrison 2008) is especially problematic in models that neglect subgrid microphysics effects, such as the numerical model used here. Nevertheless, it is clear that the distribution of E_c changes considerably with changes in Δx . The impacts of these changes, and feedbacks with other microphysical processes, are addressed in the following subsection.

a. Microphysical processes

Figure 4 shows the domain-total surface precipitation rate (R), which increases rapidly during the first 6 h of the simulations. Values of R are notably lower for the $\Delta x = 4\text{-km}$ runs over the first several hours of the simulations. A similar lag in development is seen in other variables such as maximum updraft velocity and cold pool intensity (not shown). This slower development is consistent with larger (and thus slower growing) convection, which was addressed in detail by Weisman et al. (1997, e.g., their section 5).

For $t > 6 \text{ h}$, values of R are similar between the 4- and 1-km runs, but are clearly smaller for the 0.25-km runs.

Total accumulated precipitation over the final 3 h of all simulations is listed in Table 2; precipitation tends to be largest in the $\Delta x = 4\text{-}$ and 1-km simulations, regardless of microphysical setup. For any given microphysical setup, precipitation is 10%–30% lower in the 0.25-km runs (compared to the 1-km runs).

Differences in surface precipitation rate can be explained by the competing effects of condensation (which, by itself, would tend to increase precipitation) and evaporation (which would decrease precipitation, all else being equal). Other processes that could affect the condensate budget—such as a net change in total condensate in the domain, or numerical sources/sinks of water mass—have been investigated for this case and we find them to be negligible components of the water budget for $t > 6 \text{ h}$. Hence, changes in rainfall can be explained by changes in condensation and evaporation in this case.

Total condensation (see last section of Table 3) is defined here as the sum of all vapor-to-condensate processes (including deposition). Total condensation is weakly dependent on Δx , although we note that the differences in total condensation between some 1- and 0.25-km simulations are very similar to the differences in total rainfall

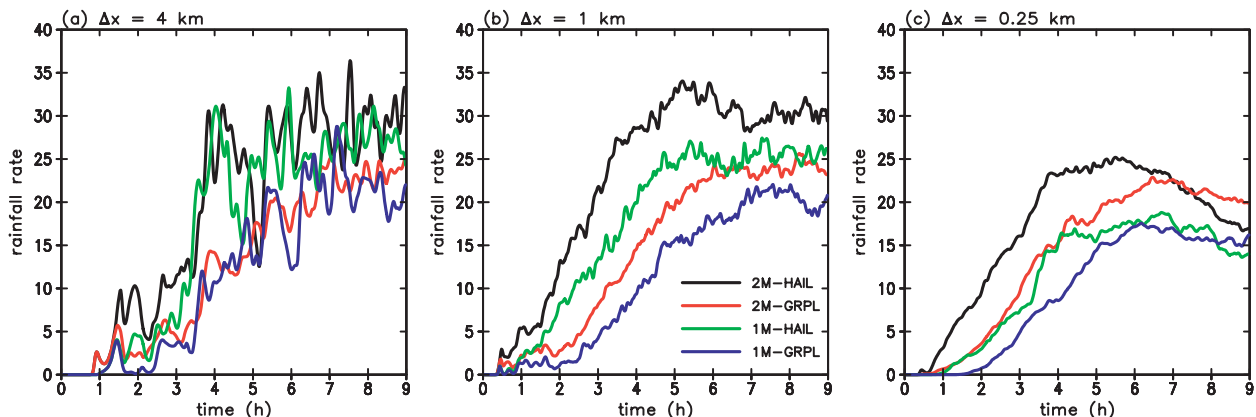


FIG. 4. Time series of domain-total rainfall rate ($\times 10^6 \text{ kg s}^{-1}$) for (a) $\Delta x = 4 \text{ km}$, (b) $\Delta x = 1 \text{ km}$, and (c) $\Delta x = 0.25 \text{ km}$. The different microphysical setups are in different colors, as indicated by the legend.

(cf. Table 2 with last section of Table 3). The 1-km simulations have the largest condensation (by $\sim 10\%$) for all configurations.

Considering evaporation rates, there is a fairly small sensitivity of rainwater evaporation E_r to Δx (first section of Table 4). Sublimation has a greater sensitivity to Δx , but the 1-km runs always have the highest values for a given microphysics setup (third section of Table 4). However, cloud water evaporation E_c has the greatest sensitivity to Δx (second section of Table 4); it increases by 20%–40% from the 4-km runs to the 1-km runs, and it increases by another 40%–50% from the 1-km runs to the 0.25-km runs. The E_c accounts for more than 50% of the total evaporation for $\Delta x = 0.25 \text{ km}$ (final section of Table 4). This result is consistent with the preceding discussion of the effects of Δx on cloud size and number of clouds, and hence on E_c .

We note that the similarity of surface precipitation between the $\Delta x = 4$ - and 1-km simulations is actually attributable to compensating effects: there is higher total condensation for $\Delta x = 1 \text{ km}$, but there is also greater total evaporation for $\Delta x = 1 \text{ km}$. These results are summarized by precipitation efficiency, defined here simply as the total precipitation divided by total condensation in the quasi-steady period (Table 5). Despite similar values of total condensation (which are all within $\sim 10\%$), the precipitation efficiency is quite different for the three values of Δx studied here.

TABLE 2. Domain-total surface precipitation ($\times 10^{11} \text{ kg}$): $t = 6$ –9 h.

Δx (km)	2M-HAIL	2M-GRPL	1M-HAIL	1M-GRPL
4	3.2	2.4	2.9	2.3
1	3.3	2.6	2.7	2.2
0.25	2.2	2.3	1.8	1.7

b. System intensity

A key question for operational applications of numerical models is, what biases are incurred by using different values of Δx . The answer is important for forecasters because Δx in operational NWP systems is determined primarily by available computing resources. We investigate some biases in this subsection by examining several different measures of squall-line intensity, which are provided in Table 6 and are explained below. We evaluate these metrics in the 6–9-h time period when the squall lines are in a statistically steady state.

The domain-total upward flux of dry air is calculated as follows: $M = \sum \rho \max(w, 0) \Delta x^2$, where ρ is the dry-air density, and the summation is over every model grid point. Values of M (first section of Table 6) are largest for $\Delta x = 1 \text{ km}$ (regardless of microphysical configuration).

Maximum updraft velocity (w_{\max}) is determined once per minute during the simulations, from anywhere in the domain; it is then averaged from $t = 6$ –9 h. Similar to

TABLE 3. Domain-total condensation/deposition ($\times 10^{11} \text{ kg}$): $t = 6$ –9 h.

Δx (km)	2M-HAIL	2M-GRPL	1M-HAIL	1M-GRPL
Condensation (vapor to cloud water)				
4	7.5	7.6	8.3	8.7
1	8.5	8.9	9.6	9.7
0.25	7.4	8.2	8.8	9.3
Deposition (vapor to ice, snow, and graupel/hail)				
4	1.8	2.1	2.1	2.5
1	2.1	2.7	2.7	3.1
0.25	1.8	2.2	2.6	2.9
Total (condensation + deposition)				
4	9.3	9.7	10.4	11.2
1	10.6	11.6	12.3	12.8
0.25	9.2	10.4	11.4	12.2

TABLE 4. Domain-total evaporation/sublimation ($\times 10^{11}$ kg): $t = 6\text{--}9$ h.

Δx (km)	2M-HAIL	2M-GRPL	1M-HAIL	1M-GRPL
Evaporation of rainwater				
4	1.9	2.4	2.4	3.1
1	2.2	2.6	2.9	3.2
0.25	1.7	2.0	2.5	2.6
Evaporation of cloud water				
4	2.4	2.4	2.7	3.0
1	2.9	3.3	3.7	4.1
0.25	4.1	4.9	5.2	6.0
Sublimation of ice, snow, and graupel/hail				
4	1.8	2.6	2.4	2.9
1	2.3	3.2	3.0	3.5
0.25	1.3	1.6	2.1	2.1
Total (evaporation + sublimation)				
4	6.1	7.4	7.6	8.9
1	7.4	9.1	9.5	10.8
0.25	7.2	8.4	9.7	10.7

M , values of w_{\max} (second section of Table 6) are at a maximum for $\Delta x = 1$ km.

Cold pool intensity is quantified by the parameter C , determined by the formula $C^2 = \int_0^h B dz$, where B is buoyancy and h is the height at which B first becomes zero. Throughout this article, buoyancy is calculated in the standard way: $B = g[(\theta - \bar{\theta})/\bar{\theta} + 0.608(q_v - \bar{q}_v)]$, where θ is potential temperature, q_v is the water vapor mixing ratio, g is gravitational acceleration, and overbars denote values from a one-dimensional reference profile. Liquid and solid water content are neglected herein to allow comparison to observations (shown later). Unless specified otherwise, the reference profile is the initial sounding (Fig. 1). The $\Delta x = 1$ -km simulations have the largest values of C for every microphysical setup (third section of Table 6), although values for $\Delta x = 0.25$ km are similar.

System propagation speed u_p is determined by first calculating line-averaged fields of perturbation potential temperature ($\theta - \bar{\theta}$) and then tracking the -1 -K value at the lowest model level. Consistent with values of C , the values of u_p (fourth section of Table 6) are largest with $\Delta x = 1$ km, although values for $\Delta x = 0.25$ km are similar.

Maximum perturbation winds at the lowest model level (u') are determined by first calculating line-averaged fields of line-perpendicular velocity (u), and then subtracting the value from $t = 0$. Maximum values of u' (fifth section of Table 6) are largest for $\Delta x = 0.25$ km.

Finally, maximum cloud top (Z_c) is determined by first calculating line-averaged fields of the cloud-ice mixing ratio (q_i), and then finding the highest level at which q_i exceeded a threshold value (10^{-5} herein). Results were similar if we used other methods, such as excluding line

TABLE 5. Precipitation efficiency (%), defined as total precipitation ($t = 6\text{--}9$ h) divided by total condensation/deposition ($t = 6\text{--}9$ h).

Δx (km)	2M-HAIL	2M-GRPL	1M-HAIL	1M-GRPL
4	34	25	28	21
1	31	22	22	17
0.25	24	22	16	14

averaging, or using relative humidity instead of q_i . Results in Table 6 (sixth section) show that the $\Delta x = 1$ -km simulations have the highest cloud tops.

Clearly, the $\Delta x = 1$ -km simulations stand out: for almost all traditional measures of squall-line intensity, the $\Delta x = 1$ -km simulations produce the most intense squall line. In terms of the weakest squall line, sometimes $\Delta x = 4$ km is weakest (i.e., maximum updraft, cold pool intensity, surface winds), but sometimes $\Delta x = 0.25$ km is weakest (surface precipitation, cloud-top height).

For changes in Δx between 4 and 1 km, the changes in squall-line intensity are likely attributable to the greater intensity of nonhydrostatic processes, owing to changes in

TABLE 6. Measures of squall-line intensity: M is total upward flux of dry air, w_{\max} is maximum vertical velocity, C is cold pool intensity, u_p is system propagation speed, u' is maximum line-averaged perturbation wind speed at the lowest model level, and Z_c is maximum cloud top. (See text for further explanation.) All variables are averaged from $t = 6\text{--}9$ h. The bold numbers highlight the largest value for a given microphysical setup. The numbers in italics indicate that the value is statistically different from the 2M-HAIL/ $\Delta x = 0.25$ -km value at the 99% confidence level.

Δx (km)	2M-HAIL	2M-GRPL	1M-HAIL	1M-GRPL
M ($\times 10^{12}$ kg s $^{-1}$)				
4	<i>0.73</i>	<i>0.75</i>	<i>0.78</i>	<i>0.79</i>
1	0.88	0.92	0.98	0.98
0.25	0.66	0.68	0.76	0.76
w_{\max} (m s $^{-1}$)				
4	28.8	30.0	28.8	31.5
1	55.4	60.3	58.1	59.9
0.25	52.9	49.6	55.0	52.3
C (m s $^{-1}$)				
4	30.8	31.6	33.3	34.3
1	35.0	36.2	37.0	37.2
0.25	33.7	35.8	36.6	36.6
u_p (m s $^{-1}$)				
4	16.4	16.7	17.4	18.1
1	19.9	19.9	20.6	20.0
0.25	19.2	19.2	19.8	19.8
u' (m s $^{-1}$)				
4	14.0	14.0	14.5	14.6
1	17.4	16.7	17.4	17.2
0.25	17.9	18.2	18.7	18.4
Z_c (km)				
4	15.4	15.4	15.6	15.9
1	15.7	15.9	16.0	16.5
0.25	13.8	13.5	14.1	13.9

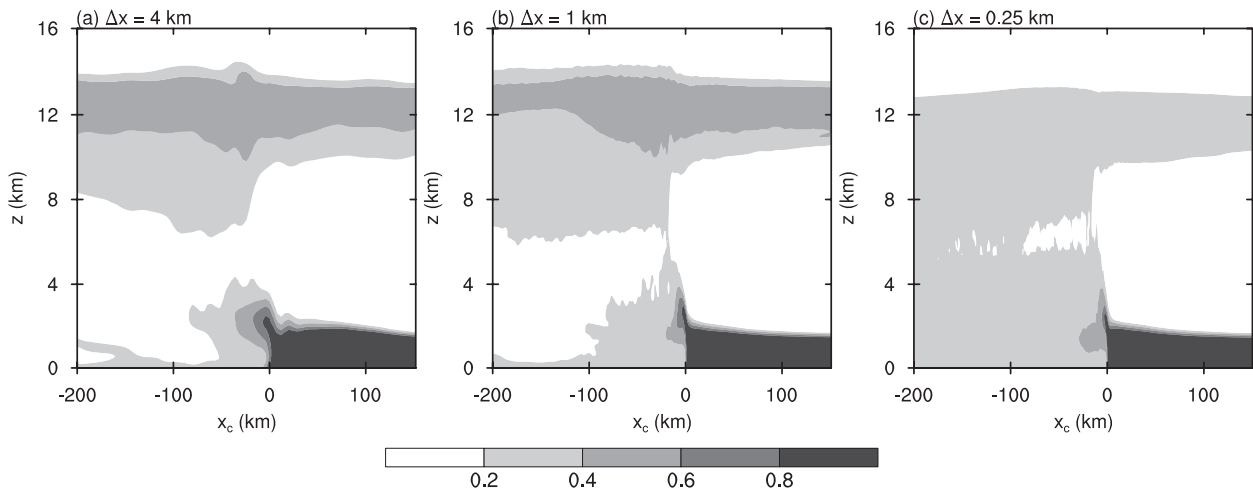


FIG. 5. Line-averaged vertical cross sections of the mixing ratio (g g^{-1}) of a passive fluid tracer (originally released in the pre-squall-line boundary layer) at $t = 9$ h for 2M-HAIL using (a) $\Delta x = 4$ km, (b) $\Delta x = 1$ km, and (c) $\Delta x = 0.25$ km.

cell size, as explained by Weisman et al. (1997). Indeed, the changes in updraft size shown in Figs. 2 and 3 are consistent with changes in nonhydrostatic pressure perturbation, such that the narrower updrafts have larger vertical accelerations, and thus larger w_{max} (e.g., section 2.11 of Cotton et al. 2011).

For changes in Δx between 1 and 0.25 km, the changes in squall-line intensity are likely attributable to the development of *resolved* turbulence, which leads to an increase in total (resolved plus parameterized) entrainment, as explained by Bryan et al. (2003). To evaluate entrainment processes, and their impact on squall-line structure, we include a passive fluid tracer in our simulations. This tracer is integrated using the same numerical techniques as the water constituents (i.e., the same advection and subgrid turbulence schemes), but there are no sources/sinks and no sedimentation. The tracer is initialized with a constant value of mixing ratio (1 g g^{-1}) in the pre-squall-line environment and only for $z < 1.5$ km (i.e., in the boundary layer), but is zero everywhere else. After 9 h (Fig. 5) the final distribution of the passive tracer is notably different for the three different grid spacings. The relatively low-resolution runs, which do not explicitly resolve turbulence/entrainment, have almost no tracer in midlevels (3–6 km AGL) (Figs. 5a,b). In contrast, the $\Delta x = 0.25$ -km run has a significant tracer throughout most of the troposphere (Fig. 5c). Compared to the highest-resolution simulation, the lower-resolution simulations deposit more tracer in the upper troposphere and lower stratosphere. While some of these differences are probably attributable to different updraft transport properties (e.g., different updraft width), a large part of these differences is likely attributable to different entrainment/mixing in the convective updrafts. That is, consistent with

observational studies (e.g., Blyth et al. 1988), turbulent eddies act to mix boundary layer air with midlevel air, and the mixture then detrains into midlevels. This process is evident in animations of the 0.25-km simulations, but not for $\Delta x \geq 1$ km.

One of the most notable impacts of Δx for these simulations is the greater cloud-top height (Z_c) for $\Delta x \geq 1$ km (Table 6). The larger values of Z_c are consistent with a lack of entrainment in convective cells. There are other impacts as well: for example, the amount of cloud ice in upper levels is considerably lower in magnitude with $\Delta x = 0.25$ km (not shown). These impacts on anvil characteristics are likely to have implications for radiative transfer, which we plan to address in future work.

Further details on turbulent processes in simulated squall lines are available in Bryan et al. (2003). We note that overall conclusions from their study (which neglected ice microphysics) seem to be unaffected by the inclusion of ice microphysical processes herein. We also note that the primary conclusions drawn in this section are independent of the microphysical setup chosen. For example, the $\Delta x = 0.25$ -km simulations produce the least rainfall and the lowest cloud tops for any microphysical setup. Thus, it seems that any of these microphysical setups can be used successfully for resolution sensitivity tests, at least for this case.

4. Sensitivity to microphysics

We now turn our attention to microphysical sensitivities. The setups of the four primary microphysical configurations are summarized at the top of Table 7. At certain places below, we present additional sensitivity experiments in support of conclusions drawn in this section. These

TABLE 7. Summary of all microphysical sensitivity simulations in this study. All simulations use 2M ice crystals and 1M cloud water (with fixed number concentration of 300 cm^{-3}).

Name	Rain	Snow	Graupel–hail	Notes
2M-HAIL	2M	2M	2M (hail)	
2M-GRPL	2M	2M	2M (graupel)	
1M-HAIL	1M	1M	1M (hail)	
1M-GRPL	1M	1M	1M (graupel)	
2M-HAIL-1MR	1M	2M	2M (hail)	
2M-GRPL-1MR	1M	2M	2M (graupel)	
2M-HAIL-D400	2M	2M	2M (hail)	Uses graupel-like density
2M-HAIL-FG	2M	2M	2M (hail)	Uses graupel-like fall velocity

additional simulations are explained at appropriate locations below, and are listed in the bottom half of Table 7.

The evolution of reflectivity at the lowest model level is shown in Fig. 6 for the four primary microphysical setups. (The calculation of reflectivity from model output is described in the appendix.) Significant differences in reflectivity structure are evident. Trailing stratiform precipitation is obviously reaching the surface in the 2M simulations, as early as $t = 4 \text{ h}$ for the 2M-HAIL configuration (Fig. 6a). The trailing stratiform region becomes wider through time in both 2M simulations (Figs. 6a,b). However, the existence of trailing stratiform precipitation near the surface remains unclear throughout the 1M simulations (Figs. 6c,d). The impact of 2M versus 1M microphysics on the trailing stratiform region is consistent with other recent modeling studies of mesoscale convective systems (Morrison et al. 2009; Luo et al. 2010). The only simulation with an obvious transition region—that is, weak (but nonzero) reflectivities between the stratiform and convective regions—is the 2M-HAIL simulation (Fig. 6a).

We find that two microphysical processes are primarily responsible for these differences in system structure: 1) the raindrop size distribution and 2) the specification of hail or graupel. These two topics are discussed in the following two subsections.

a. The importance of raindrop size distribution

A notable difference between 1M and 2M is the decrease in reflectivity below the melting level for 1M (Figs. 7c,d), but nearly constant reflectivity with height for 2M (Figs. 7a,b). Differences in rainwater evaporation (E_r ; contours in Fig. 7) are responsible for these patterns of reflectivity; that is, E_r is higher in the 1M simulations than the 2M simulations.

The relatively lower values of E_r for 2M are associated with different representations of the raindrop size distribution. In 2M, N_{or} is a parameter predicted from the forecasted rain mixing ratio and number concentration. In 1M, it is specified as a constant $N_{or} = 10^7 \text{ m}^{-4}$ (see Table 1). A line-average cross section of the predicted N_{or}

from 2M is shown in Fig. 8. The predicted values of N_{or} from 2M are larger in the convective region and smaller in the trailing stratiform region (indicating variations in mean drop diameter and/or drop concentration). For a given rain mixing ratio, a larger N_{or} means a greater evaporation rate (because the total surface area is larger), and hence E_r is lower in the stratiform region in 2M. There is also an increase in N_{or} with height (below the melting level), which mostly reflects size sorting.

This overall distribution of N_{or} in 2M is consistent with disdrometer observations (Waldvogel 1974; Tokay and Short 1996; Atlas et al. 1999; Uijlenhoet et al. 2003). Specifically, the transition from large values in the convective region to smaller values in the trailing stratiform region has been noted in several studies, and has been termed the “ N_0 jump.” A key point is that this distribution is captured by physical processes operating in 2M. No single value of N_{or} specified in 1M is able to capture the N_0 jump. Furthermore, as described by Morrison et al. (2009), tuning N_{or} in 1M to values predicted in a particular region of the storm would produce biases in other regions.

To check whether the raindrop size distribution was primarily responsible for the differences in the trailing stratiform region between our 1M and 2M simulations, we ran additional simulations that retained 2M for snow and hail/graupel, but used 1M for rain (see 2M-HAIL-1MR and 2M-GRPL-1MR in Table 7). These simulations produce qualitative results very similar to simulations that use 1M for all species (Fig. 9). In particular, there is a rapid decrease of reflectivity toward the surface in cross sections of reflectivity (Fig. 9). These results are consistent with the findings of Morrison et al. (2009), who conducted two-dimensional simulations of a squall line, and of Luo et al. (2010), who conducted three-dimensional simulations of mesoscale convective systems.

b. Hail versus graupel

Another important microphysical sensitivity explored in this study is the impact of using graupel- or hail-like characteristics for the rimed ice species. This subject has been investigated in previous studies, mostly in

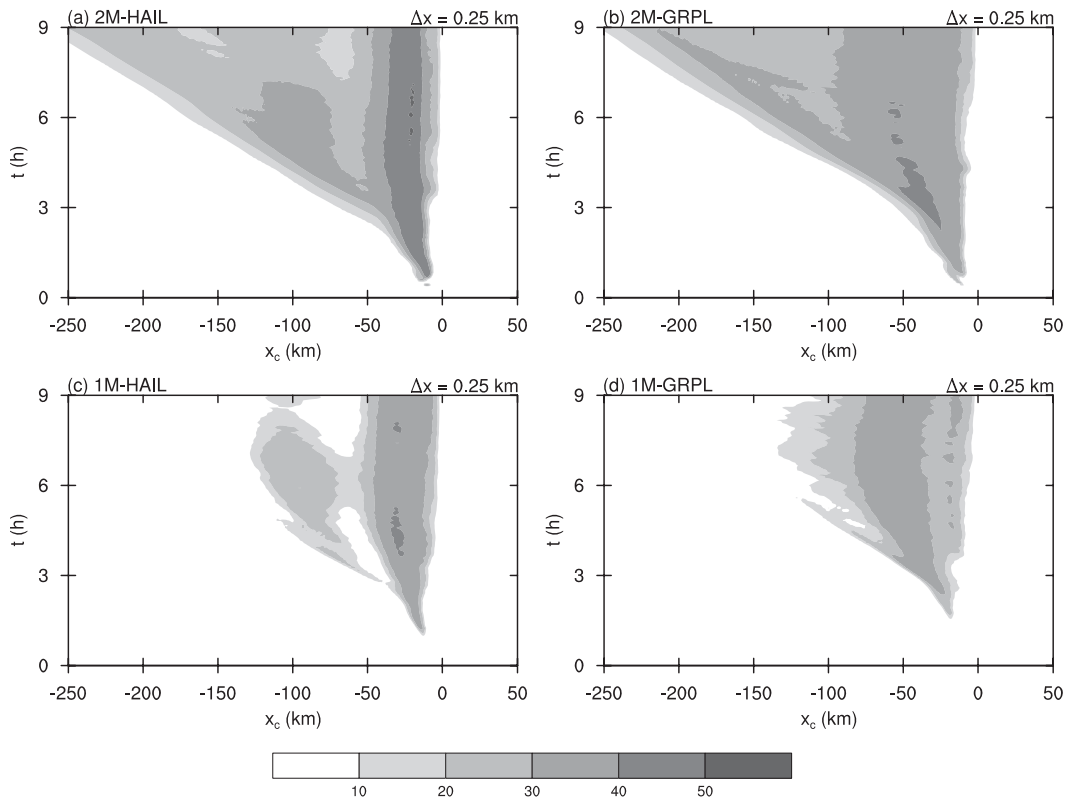


FIG. 6. Hovmöller diagrams of line-averaged reflectivity (dBZ) at the lowest model level using $\Delta x = 0.25$ km for (a) 2M-HAIL, (b) 2M-GRPL, (c) 1M-HAIL, and (d) 1M-GRPL.

the context of supercell storms (Gilmore et al. 2004b; VanWeverberg et al. 2010; Morrison and Milbrandt 2011). These studies found that the simulated storm characteristics, including surface precipitation and a cold pool, were sensitive to the specification of either graupel or hail characteristics. Fewer studies have explored this issue in the context of squall-line simulations. McCumber et al. (1991) found that specifying characteristics of graupel instead of hail resulted in greater realism for a tropical squall line observed in the western Pacific.

In our simulations, using graupel as the rimed ice species results in a considerably wider region of high reflectivity associated with the main line of convection (compared to simulations with hail) (Figs. 6, 7). For simplicity, we define the convective region as reflectivity >30 dBZ in the area just behind the surface gust front: thus defined, the convective region is $\sim(50\text{--}80)$ km wide for GRPL, but only ~ 30 km wide for HAIL. The width of the convective region of the observed squall line was roughly 30 km (see Figs. 3, 4 of BP10). Peak reflectivities in the convective region are also higher, and more consistent with the observed case, with HAIL (~ 55 dBZ) compared to GRPL (~ 45 dBZ). Furthermore, the low-reflectivity transition region is clearly captured when using

hail, but not with graupel. Overall, the 2M-HAIL simulation produces results that are closer to observations (cf. Figs. 3, 4 of BP10). Another notable difference between GRPL and HAIL is that vertical cross sections show peak reflectivities in the convective region well above the surface for GRPL, but near the surface (and more similar to observations) for HAIL (Fig. 7).

We reiterate that the only differences for specification of either hail or graupel are the fall speed relation and the bulk density (see section 2b). We note that in reality these parameters are generally not independent, though they are specified independently in nearly all bulk microphysics schemes. Additional sensitivity tests using 2M-HAIL, but with either the fall speed relation or bulk density modified to that of graupel, are performed to see which change has the most impact (see 2M-HAIL-D400 and 2M-HAIL-FG in Table 7). Figure 10 shows line-averaged cross sections of radar reflectivity for these two simulations at $t = 9$ h. The simulation with modified bulk density exhibits a reflectivity structure similar to 2M-HAIL (cf. Figs. 7a, 10a), whereas the test with a modified fall speed relation is similar to 2M-GRPL (cf. Figs. 7b, 10b). These results indicate that the fall speed relation has more impact than bulk density in terms of specification of rimed

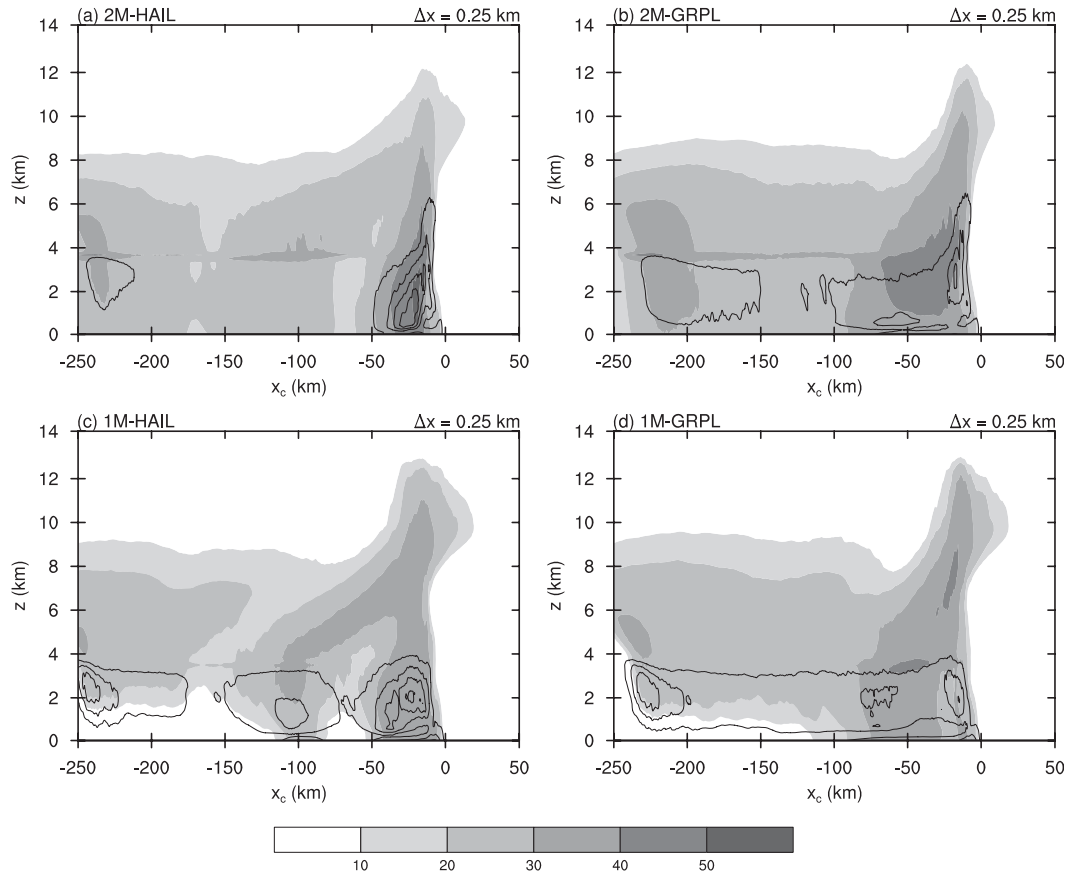


FIG. 7. Line-averaged vertical cross sections of reflectivity (dBZ; shaded) at $t = 9$ h using $\Delta x = 0.25$ km for (a) 2M-HAIL, (b) 2M-GRPL, (c) 1M-HAIL, and (d) 1M-GRPL. Rainwater evaporation rate is contoured at the following levels: $1, 3, 5, 7$, and $9 \times 10^{-7} \text{ kg kg}^{-1} \text{ s}^{-1}$.

ice characteristics for graupel or hail. This finding is consistent with Morrison and Milbrandt (2011), who found that changes in fall speed relation for graupel versus hail had a larger impact than changes in bulk density on surface precipitation and cold pool characteristics of a supercell storm.

Results here differ from the conclusions of McCumber et al. (1991), who studied a tropical squall line. We expect hail to be much less prevalent in weaker convection typical of tropical maritime environments. Nonetheless, they found that inclusion of graupel rather than hail in a one-moment scheme with three ice species produced

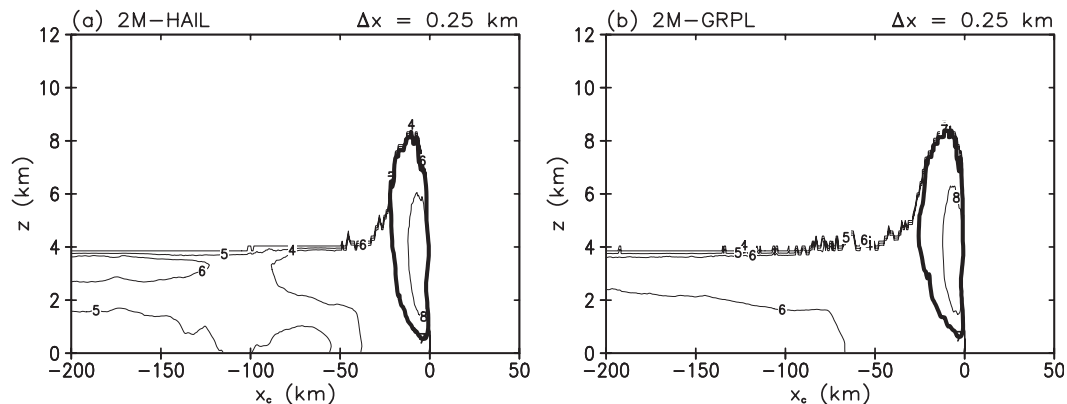


FIG. 8. Line-averaged cross sections of $\log_{10}(N_{or})$ at $t = 9$ h from (a) 2M-HAIL and (b) 2M-GRPL. The thick contour is $N_{or} = 10^7$, which is the value specified for the 1M simulations.

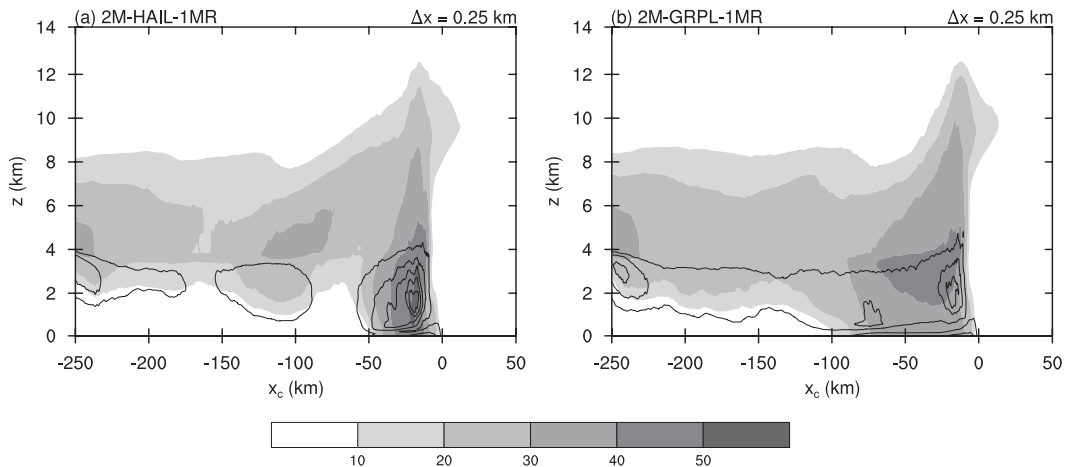


FIG. 9. As in Fig. 7 but for (a) 2M-HAIL-1MR and (b) 2M-GRPL-1MR (see Table 7 for more information).

the most realistic results. It is unclear if differences between the current study and that of McCumber et al. are due to different environments (midlatitude versus tropical), differences in microphysics schemes, or differences in other aspects of the numerical models. In future work we plan to extend the current study to include tropical squall-line simulations.

c. Impact of resolution on microphysical sensitivities

In terms of overall system structure, for any value of Δx we find similar sensitivities to 1M versus 2M and to HAIL versus GRPL. For example, all 2M runs show more realistic trailing stratiform regions (with precipitation reaching the surface), whereas all 1M simulations do not. Also, the convective region is significantly wider with GRPL than with HAIL (although this result is less obvious for $\Delta x = 4$ km than for the other resolutions) (not shown).

However, at any *specific time*, there are notable differences in reflectivity structure with different Δx ; these differences are a consequence of slower storm development in the lower-resolution simulations, especially for $\Delta x = 4$ km. For example, Hovmöller diagrams of reflectivity show that the 2M runs develop a trailing stratiform region that reaches the surface (Figs. 11a,b), while the 1M runs have excessive evaporation in the trailing stratiform region such that precipitation does not reach the surface (Figs. 11c,d). (In this figure, regions with contours but not shading indicate reflectivity above the ground but not at the ground.) Clearly apparent in Fig. 11 is the much slower development of a trailing stratiform region with $\Delta x = 4$ km, which is attributable to the much larger cell size, as discussed in section 3. Hence, in terms of overall qualitative results, we reach the same overall conclusions about microphysical sensitivities for any specified value of Δx . This result suggests

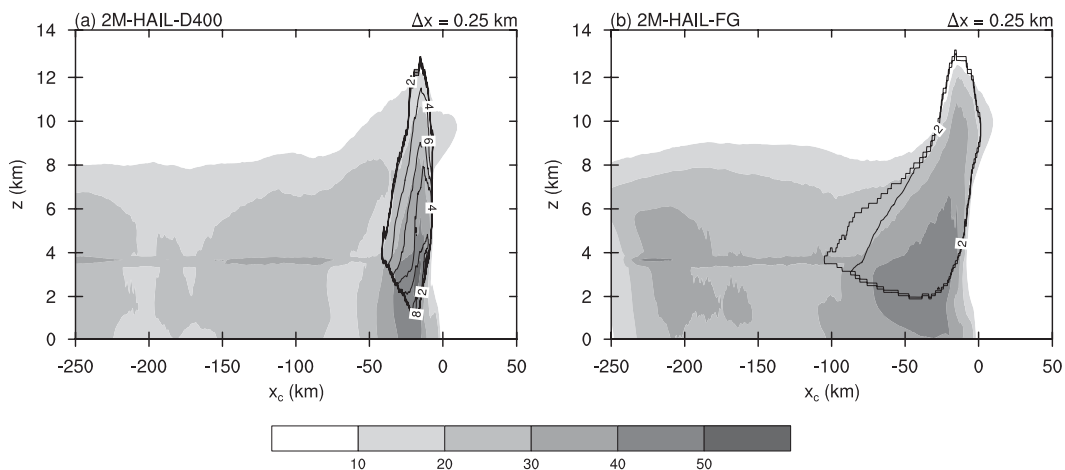


FIG. 10. Line-averaged cross sections of reflectivity (shaded) and fall velocity of hail/graupel (contours; every 1 m s⁻¹) for (a) 2M-HAIL-D400 and (b) 2M-HAIL-FG (see Table 7 for more information).

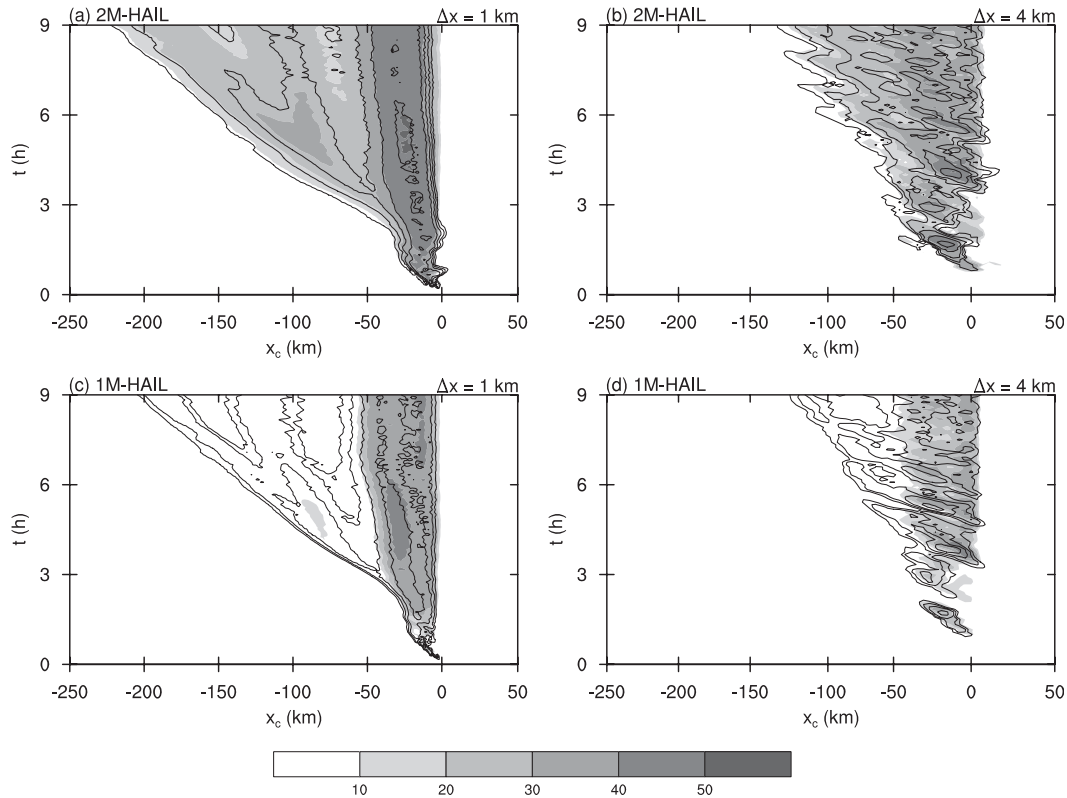


FIG. 11. Hovmöller diagrams of line-averaged reflectivity (dBZ) at the lowest model level for (a) 2M-HAIL with $\Delta x = 1$ km, (b) 2M-HAIL with $\Delta x = 4$ km, (c) 1M-HAIL with $\Delta x = 1$ km, and (d) 1M-HAIL with $\Delta x = 4$ km. Contours show reflectivity at $z = 3$ km (contour interval is 10 dBZ).

that any value of Δx between 0.25 and 4 km can be used for microphysical sensitivity tests, although caution must be taken to account for slower evolution with $\Delta x = 4$ km.

5. Comparison to VORTEX2 analyses

Clearly, horizontal grid spacing (Δx) and microphysics configuration (1M versus 2M and/or HAIL versus GRPL) have significant impacts on squall-line properties such as reflectivity structure, surface rainfall, cold pool characteristics, etc. To help determine which model configuration produces the most realistic simulation, we compare against the high-temporal-resolution rawinsondes launched during VORTEX2. Here, we use the mesoscale analyses of the sounding data that were presented by BP10. Details are available in BP10, although we note that they used a two-dimensional ($x_c - z$) grid, where x_c is the distance normal to the surface gust front. The grid spacing for these analyses was 10 km in the horizontal and 100 m in the vertical.

We do not perform any rigorous quantitative evaluation of the model output using VORTEX2 data for several reasons, such as the disparity in resolution, uncertainty about the representativeness of the soundings, and because of the idealization of the simulations (e.g.,

neglect of radiation, surface fluxes, and mesoscale variability). In fact, comparison with the VORTEX2 data will inevitably be subjective/qualitative because of differences in timing owing to different initiation mechanisms. Also, the observational analyses were created from soundings launched at different times (from one site as the squall line passed), and the squall line evolved somewhat during this time period. We note that the observed soundings from the convective and trailing stratiform regions of the system (S6–S9; see BP10) were launched roughly 4–5 h after the squall line first formed. Because the properties of these regions are of key interest here, we show model output averaged between 4 and 5 h. The primary purpose of the following analysis is to determine if any of the microphysical setups have any obvious shortcomings.

Line-average cross sections of relative humidity (H) w.r.t. liquid are shown in Fig. 12. In the trailing stratiform region, H is considerably lower with 2M than 1M (cf. Figs. 12a,b) because of the different rainwater evaporation rates in the trailing stratiform rain (section 4a). The lower H values from 2M compare better with observations, although all simulations are too humid at low levels in the cold pool (i.e., for $x_c < 0$ and $z < 3$ km). The model output shown here is averaged along the line, whereas the

observations are from one location; nevertheless, we find that $H < 40\%$ does not occur at any individual grid point in the cold pool of the $\Delta x = 0.25$ -km simulations, confirming a general moist bias in these simulations.

There are also notable structural differences between the simulations, which are likely attributable to the different rates of generation of the cold pool; the hail simulations (e.g., Figs. 12a,b) develop a cold pool faster, owing to the larger fall velocity of hail compared to graupel. Thus, the hail simulations develop an upshear-tilted structure more quickly, which is partly responsible for the different structure at this time compared to the run with graupel (Fig. 12c). Locations at $x_c < -50$ km in the observational analysis are at the latest time (owing to time-to-space conversion), and so differences in Figs. 12a–c are partially attributable to the different time periods.

The structural differences are more apparent for changes in grid spacing. The $\Delta x = 4$ -km simulation (Fig. 12e) is the slowest to develop, which explains the lack of a large trailing stratiform region by this time. The comparatively large cloud tops with $\Delta x \geq 1$ km are evident in Figs. 12d and 12e, but we cannot evaluate this difference using the VORTEX2 analysis owing to the lack of observations for $x_c \approx 50$ km.

Cross sections of buoyancy (relative to the initial environmental sounding) are shown in Fig. 13. The model simulations capture some observed changes of B in the environment ahead of the squall line ($x_c > 0$), such as cooling near the top of the boundary layer and in mid-levels, warming in the 8–12-km layer, and cooling in the lower stratosphere. (The model does not produce cooling near the surface in the environment because radiative processes and surface heat fluxes are neglected in this study.) In the near-surface cold pool ($x_c < 0$), B is slightly lower for 1M compared to 2M (cf. Figs. 13a,b); this difference is attributable to the enhanced E_r with 1M (discussed earlier). Using graupel instead of hail does not have much effect on the distribution or magnitude of B (cf. Figs. 13a,c). In terms of resolution sensitivity, the cold pool for $\Delta x = 4$ km is generally weaker and shallower than the analysis (cf. Figs. 13e,f), whereas the $\Delta x = 1$ -km simulation produces a similar distribution of B , but larger amplitudes, compared to the $\Delta x = 0.25$ -km run (cf. Figs. 13a,d). In all simulations, buoyancy is slightly too low near the surface because of a low bias in temperature; we cannot explain this bias, at this time, but it is probably attributable to excessive evaporation and/or the neglect of surface fluxes.

With the exception of $\Delta x = 4$ km, all simulations reproduce the observed cold pool depth h reasonably well (where h is defined as the level where B first becomes zero). In the observations and model simulations with $\Delta x \leq 1$ km, h is roughly 4 km near the surface gust front, and is roughly 4.5 km in the trailing stratiform region

(i.e., ~ 1 km above the melting level, which is shown by the dashed line).

Figures 14a,b and 14c,d show h and cold pool intensity C , respectively, for two simulations, where the thick black line is the average value, and shading encloses the minimum and maximum values within the domain. The plus symbols in Fig. 14 denote observed values (from BP10). All simulations (including those not shown) tend to underestimate h slightly in the trailing stratiform region ($x_c < -30$ km). Closer to the leading edge of the cold pool, the observed value at $x_c = 8$ km is reproduced at some grid points, although the mean value of h is slightly lower than the observed value. The very large values of h near the surface gust front ($-5 \text{ km} < x_c < 0$) are attributable to the deep layer of cool air associated with ascent in the environment (see Fig. 13) but not to precipitation processes. Analyses using the thermodynamic profile just ahead of the squall line (instead of the initial sounding) for the reference profile do not yield such large values of h (not shown).

Values of cold pool intensity C from the simulations are generally similar to the observed values (i.e., $30\text{--}35 \text{ m s}^{-1}$). However, the 2M simulations reproduce the slight decrease in C toward the rear of the trailing stratiform region (i.e., as x_c decreases), whereas the 1M simulations produce an increase in C in this region. Again, the enhanced values of E_r in the 1M runs are likely the cause of this difference.

Cross sections of line-normal system-relative flow u are shown in Fig. 15. The overall features are captured by all simulations, including upper-level outflow near the tropopause, acceleration of front–rear flow in the convective region between 3 and 8 km AGL, and rear-to-front flow (shaded) near the front edge of the cold pool. All simulations appear to lack a clear elevated rear inflow for $x_c < -50$ km and $z \approx 2$ km. However, this result may be attributable to averaging of the model output; there are, in fact, areas with $u > 0$ between 2 and 3 km AGL for all simulations (not shown), but only in isolated areas. The 1M simulations produce slightly stronger values of u in the cold pool (e.g., Fig. 15b), and more expansive areas with $u > 0$, which is consistent with their stronger cold pools.

Analyses of equivalent potential temperature θ_e (not shown) have similar overall features between model output and observations, including a nearly constant θ_e layer from the melting level to the tropopause in the trailing stratiform region, and lower values of θ_e in the cold pool. However, θ_e in the cold pool is 5–10 K *higher* in the simulations than observations. This difference is consistent with the positive H bias in the cold pool (discussed earlier). Some soundings from the trailing stratiform region are shown in Fig. 16; an observed sounding is included as thin black lines for comparison. The 2M-HAIL simulation

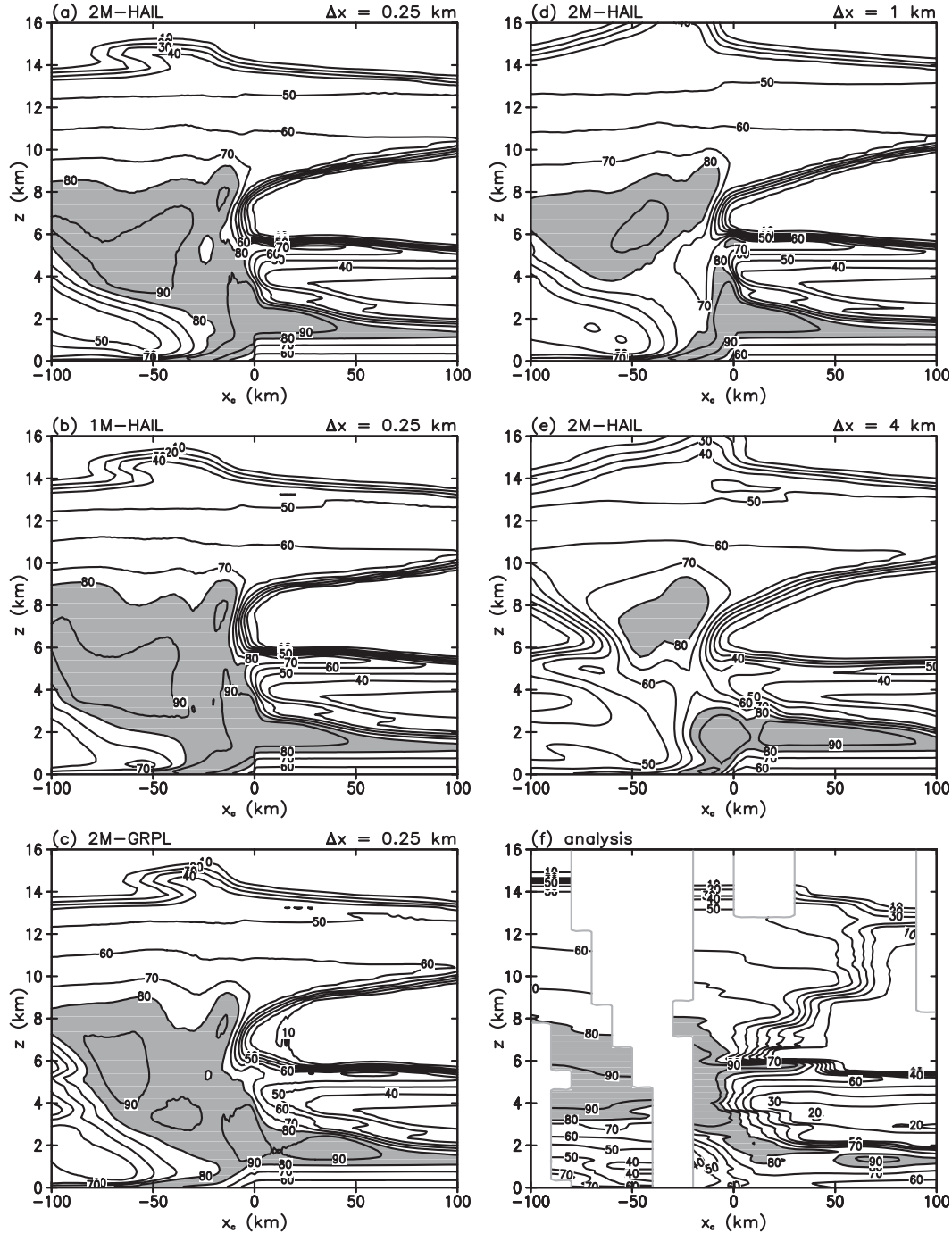


FIG. 12. Vertical cross sections of relative humidity H : line-averaged values averaged over 4–5 h for (a) 2M-HAIL with $\Delta x = 0.25$ km, (b) 1M-HAIL with $\Delta x = 0.25$ km, (c) 2M-GRPL with $\Delta x = 0.25$ km, (d) 2M-HAIL with $\Delta x = 1$ km, and (e) 2M-HAIL with $\Delta x = 4$ km. (f) The observational analysis from BP10 (where areas of insufficient data are left blank and are enclosed by gray lines). Contour interval is 10%. Values $>80\%$ are shaded.

(Fig. 16a) has a comparable temperature profile in the cold pool (below 650 mb) but is considerably moister than the observed sounding; hence, the θ_e bias is clearly related to the moist bias. The 1M-HAIL simulation (Fig. 16b) is

too moist *and* too cold below 700 mb (although near-surface conditions are close to observed values).

It is possible that the moist bias is caused by excessive diffusion in the numerical simulations. As discussed by

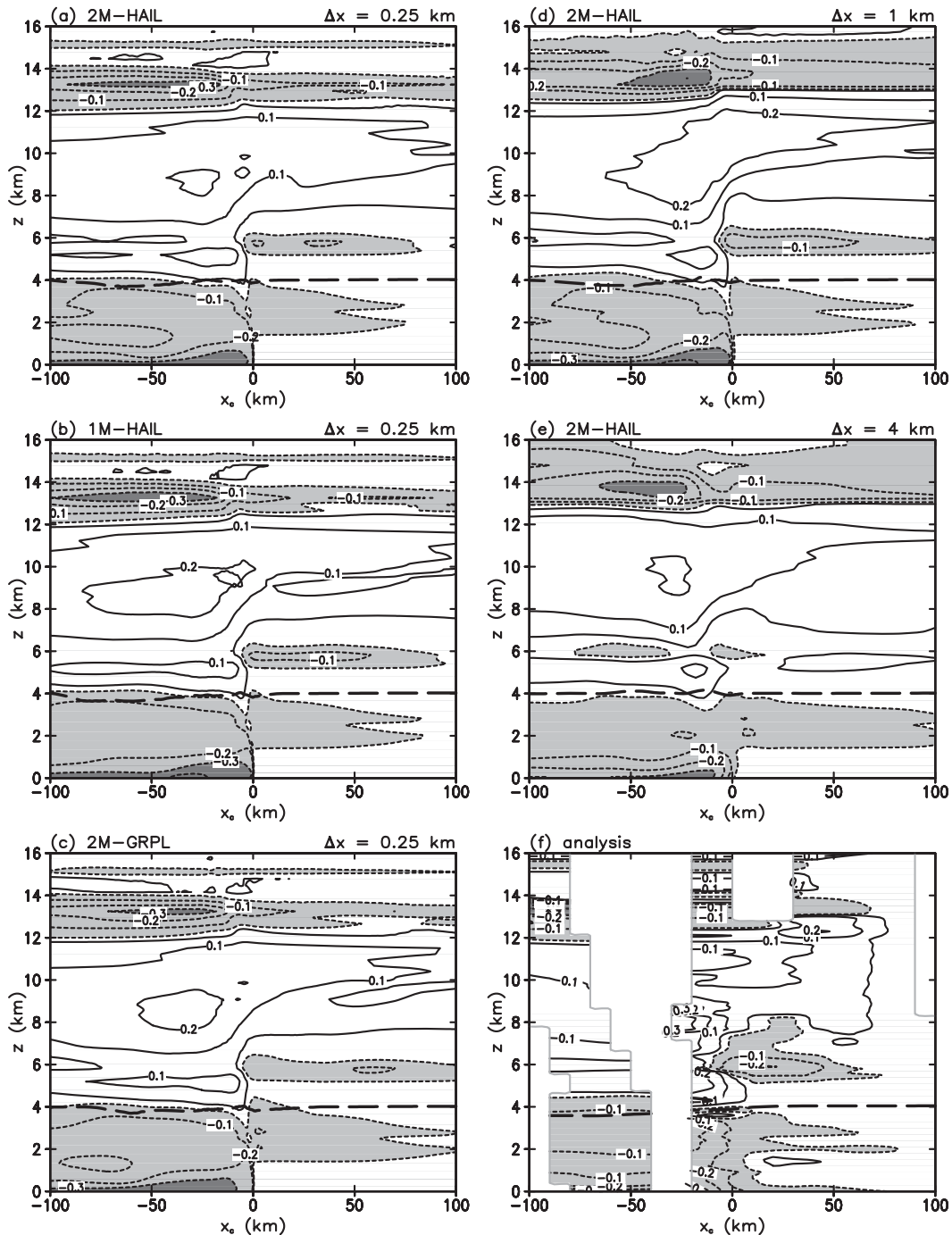


FIG. 13. As in Fig. 12, but for buoyancy B . Contour interval is 0.1 m s^{-2} , except intermediate contours of $\pm 0.02 \text{ m s}^{-2}$ are also included. The melting level is included as a thick dashed line. Light shading denotes $B < -0.02 \text{ m s}^{-2}$ and dark shading denotes $B < -0.3 \text{ m s}^{-2}$.

BP10, observed values of θ_e in the cold pool were consistent with undiluted subsaturated descent likely caused by evaporation in midlevel air. All of our simulations have air in the cold pools that originated in midlevels, but nowhere is that air undiluted; we have confirmed this

conclusion by including passive fluid tracers, originating in midlevels, in our simulations (not shown). In future studies we will examine the possible role played by microphysical sensitivities that are beyond the scope of this article, such as specified cloud drop concentration, raindrop

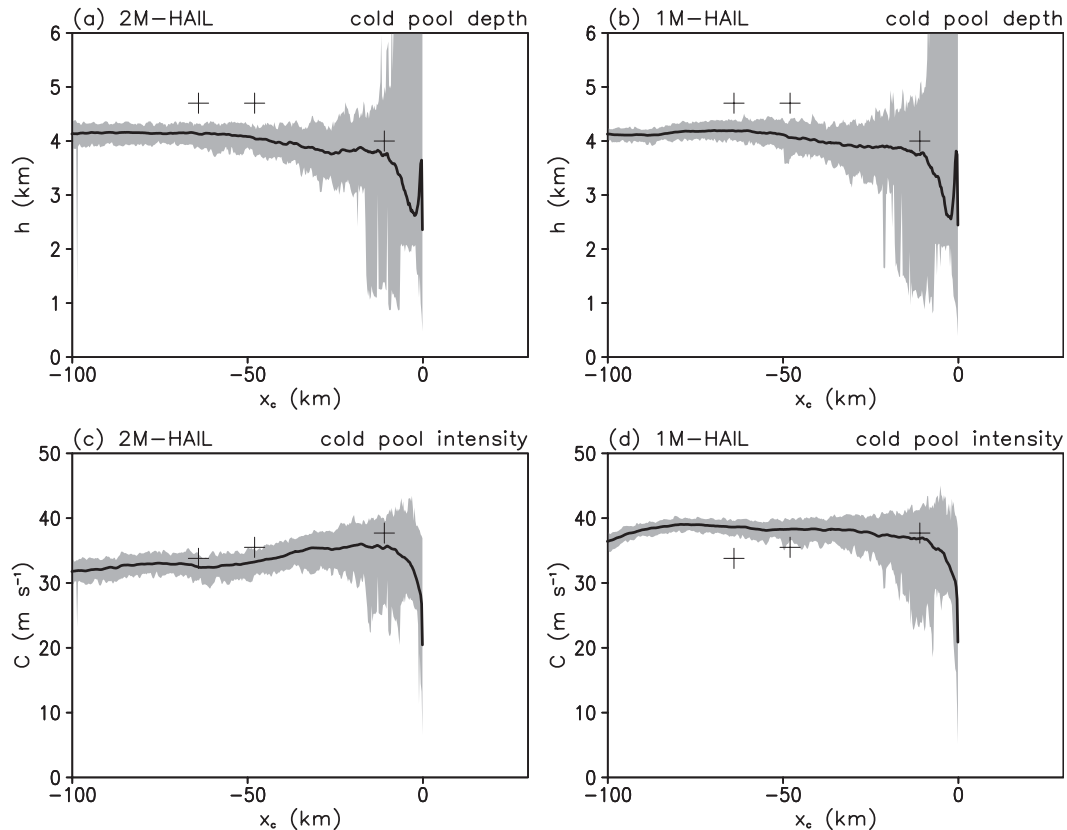


FIG. 14. Analyses of (a),(b) cold pool depth h and (c),(d) cold pool intensity C at $t = 5$ h using $\Delta x = 0.25$ km. The 2M-HAIL simulation is shown in (a) and (c) and the 1M-HAIL simulation is shown in (b) and (d). The black line shows the average value, and the shading encloses minimum and maximum values in the domain. The plus symbols are from the observational study of BP10.

breakup parameterization, etc. that may account for this moist bias.

Overall, we conclude from this comparison to the VORTEX2 analyses that all simulations produce a reasonably accurate simulation in terms of mesoscale structure; specifically, all microphysical setups produce reasonably similar cold pool structure and line-normal flow. The 2M-HAIL simulations stand out because they produce reasonable H values below the melting level in the trailing stratiform region, although this setup slightly underestimates the observed cold pool depth in this area. The $\Delta x = 4$ -km simulations are clearly slower to develop, and have weaker cold pools. In future studies, we plan to investigate model settings and/or physical parameterizations (e.g., radiation) that are needed to produce better results, but this first attempt has produced encouraging results.

6. Summary

We have conducted a series of idealized squall-line simulations using the environment of the 15 May 2009

squall line that was observed during VORTEX2. Despite the relative simplicity of the model setup (e.g., no radiative tendencies, no surface heat fluxes, and a horizontally homogeneous initial environment), the model simulations produce reasonably accurate overall squall-line structure. This study focuses on the sensitivity to changes in microphysical setup and horizontal grid spacing (Δx from 4 to 0.25 km). The changes to the microphysical setup include one-moment versus double-moment (2M) processes, and hail versus graupel as the dense (rimed) ice species.

Changes to either microphysics or Δx affect the structure and intensity of the simulated squall line. Changes to Δx have a greater impact overall than the changes in microphysical setup, although this result is partially attributable to slower spinup and evolution with the relatively coarse ($\Delta x = 4$ km) resolution. An especially notable result from this study is that surface precipitation decreases as horizontal grid spacing decreases: specifically, surface precipitation is 10%–30% lower with $\Delta x = 0.25$ km than with $\Delta x = 1$ km. This result can be explained by changes in condensation and evaporation,

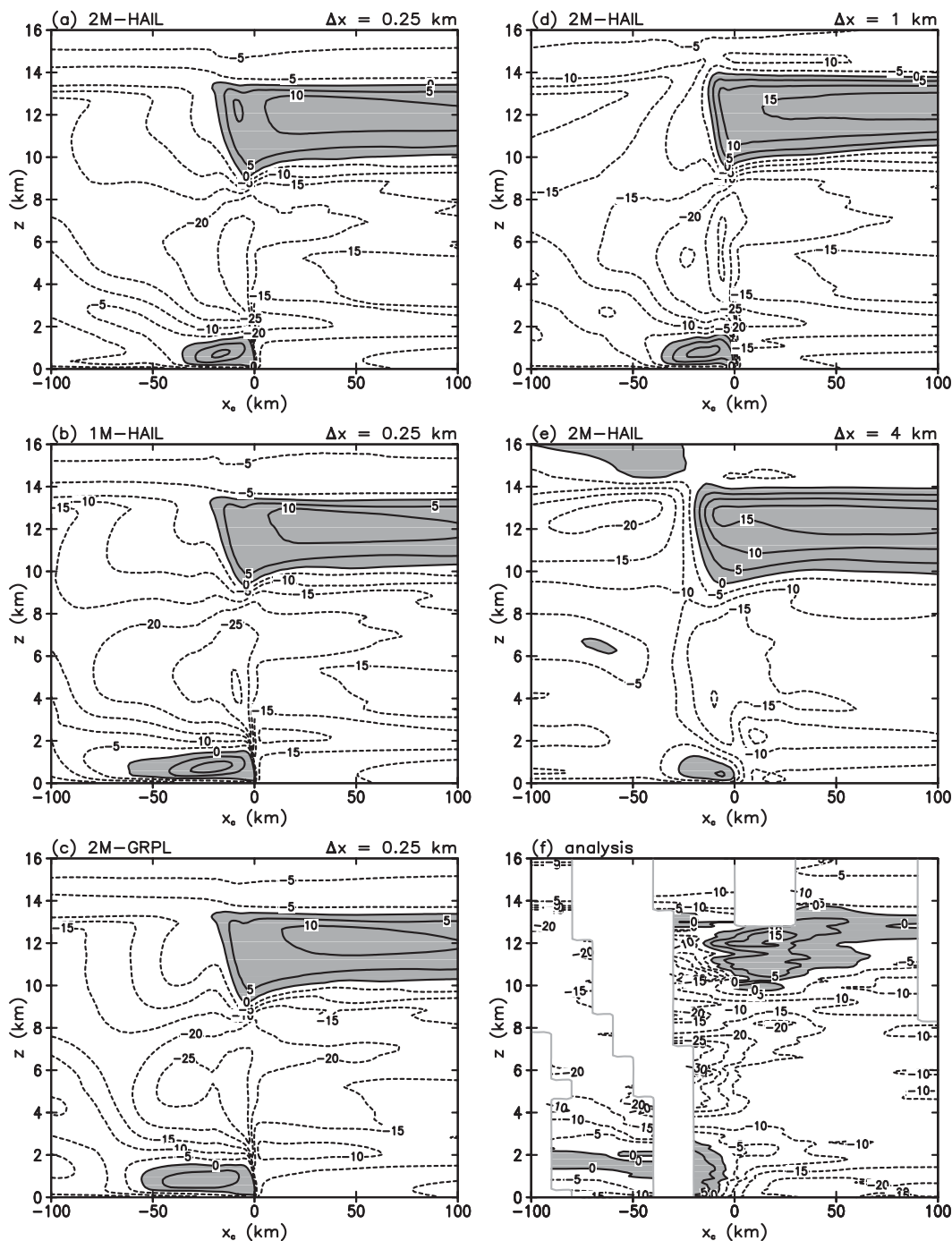


FIG. 15. As in Fig. 12, but for system-relative across-line wind speed u . Contour interval is 5 m s^{-1} . Values > 0 are shaded.

as discussed in section 3a. Most notably, decreasing Δx typically leads to larger evaporation, and most of the change is attributable to the evaporation of cloud water (not rainwater). Changes in the total surface area of clouds, and enhanced entrainment/detrainment because of resolved turbulence, seem to be primarily responsible

for the increase in cloud water evaporation with decreasing Δx .

Consistent with previous studies, we find that single-moment (1M) specification of microphysics produces less realistic results. The trailing stratiform precipitation does not exist at the surface with 1M because rainwater

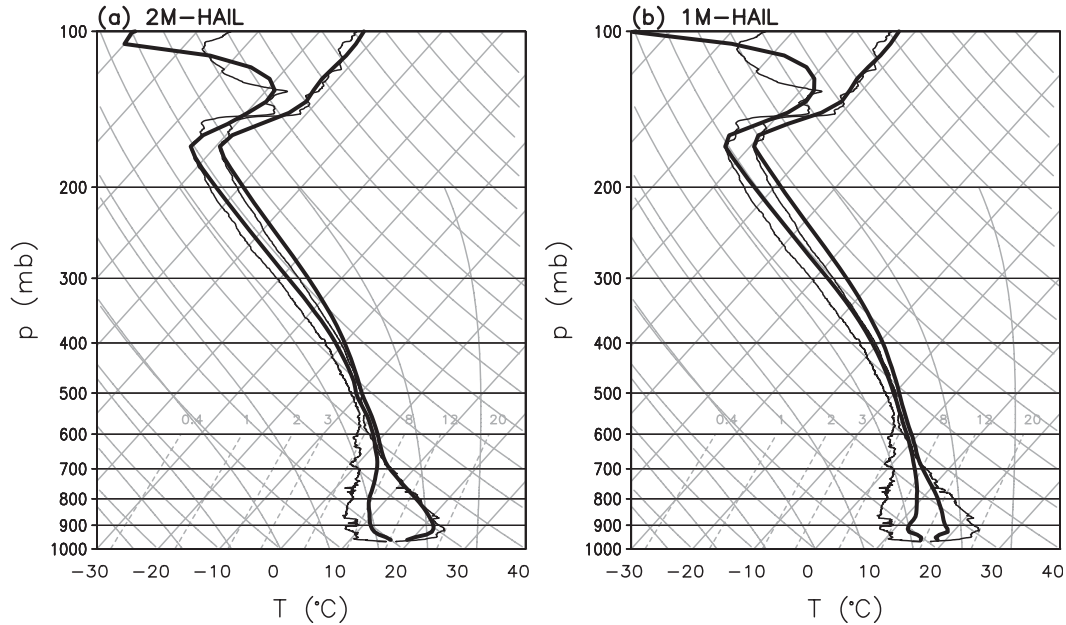


FIG. 16. Soundings at $x_c = -50$ km at $t = 5$ h using $\Delta x = 0.25$ km with (a) 2M-HAIL and (b) 1M-HAIL. The model soundings (thick lines) are averaged along the line. An observed sounding (S7 from BP10) is shown by thin lines that was launched at $x_c = -46$ km approximately 5 h after the squall line formed.

evaporates too quickly (which also accounts for a low-buoyancy bias in the cold pool, and higher relative humidity, compared to both observations and the 2M runs). Simulations with graupel (instead of hail) produce convective regions that are too wide and have lower reflectivity, which is primarily attributable to the slower fall velocity of graupel compared to hail.

Microphysical sensitivities are found to be qualitatively similar for the different grid spacings. For example, 2M simulations produce more rain and weaker cold pools compared to 1M, regardless of the value for Δx . This result suggests that model users can test microphysical sensitivity at lower resolution and get qualitatively consistent results. However, quantitative differences are apparent for higher resolution.

By comparing against rawinsonde data collected during VORTEX2, the simulation with $\Delta x = 0.25$ km, double-moment microphysics, and hail as the dense ice species is the most realistic. This run (2M-HAIL) stands out because (i) it has realistic convective, transition, and trailing stratiform regions, (ii) the depth, intensity, and distribution of the surface-based cold pool compare favorably with observations, and (iii) it has reasonably low values of relative humidity at low levels ($z < 4$ km) in the trailing stratiform region. However, *all* simulations have a positive bias in relative humidity and low bias in temperature in the cold pool, which is possibly related to excessive evaporation, but is difficult to explain definitively at this time.

Finally, we note that this study examines only one case in a relatively high-CAPE, low-shear environment. Future work should repeat these types of analyses for different cases and different environments, perhaps including lower-CAPE tropical environments and higher-shear midlatitude environments.

Acknowledgments. The authors thank Greg Thompson for providing the reflectivity code. Wojciech Grabowski and Morris Weisman provided helpful reviews of an earlier version of this manuscript. Hugh Morrison acknowledges support from NOAA Grant NA08OAR4310543, U.S. DOE ARM DE-FG02-08ER64574, and the NSF Science and Technology Center for Multiscale Modeling of Atmospheric Processes (CMMAP), managed by Colorado State University under Cooperative Agreement ATM-0425247.

APPENDIX

Technical Details

a. Details of the numerical model

The numerical model (CM1) integrates governing equations for the three Cartesian components of velocity (u , v , w), potential temperature (θ), nondimensional pressure (π), and mixing ratios for water vapor (q_v), liquid water (q_l ; i.e., cloud and rain), and solid water (q_s ; i.e.,

snow, ice, and graupel/hail). The velocity equations are reported elsewhere (e.g., Bryan and Fritsch 2002). The governing equations for moisture, potential temperature (θ), and nondimensional pressure (π) are listed here to clarify how ice processes are included:

$$\begin{aligned} \frac{\partial \theta'}{\partial t} = & -u_i \frac{\partial \theta}{\partial x_i} + D_\theta + R_\theta - \Theta_1 \theta \left(\frac{\partial u}{\partial x} + \frac{\partial v}{\partial y} + \frac{\partial w}{\partial z} \right) \\ & + \Theta_2 (L_{lv} \dot{q}_{lv} + L_{sv} \dot{q}_{sv} + L_{sl} \dot{q}_{sl}) + \Theta_3 (\dot{q}_{lv} + \dot{q}_{sv}), \end{aligned} \quad (\text{A1})$$

$$\begin{aligned} \frac{\partial \pi'}{\partial t} = & -u_i \frac{\partial \pi}{\partial x_i} - \Pi_1 \pi \left(\frac{\partial u}{\partial x} + \frac{\partial v}{\partial y} + \frac{\partial w}{\partial z} \right) \\ & + \Pi_2 (L_{lv} \dot{q}_{lv} + L_{sv} \dot{q}_{sv} + L_{sl} \dot{q}_{sl}) + \Pi_3 (\dot{q}_{lv} + \dot{q}_{sv}) \\ & + \Pi_4 (D_\theta + R_\theta) + \Pi_5 D_{qv}, \end{aligned} \quad (\text{A2})$$

$$\frac{\partial q_v}{\partial t} = -u_i \frac{\partial q_v}{\partial x_i} + D_{qv} - \dot{q}_{lv} - \dot{q}_{sv}, \quad (\text{A3})$$

$$\frac{\partial q_l}{\partial t} = -u_i \frac{\partial q_l}{\partial x_i} + D_{ql} + \dot{q}_{lv} - \dot{q}_{sl} + \frac{1}{\rho_a} \frac{\partial (\rho_a V_l q_l)}{\partial z}, \quad (\text{A4})$$

$$\frac{\partial q_s}{\partial t} = -u_i \frac{\partial q_s}{\partial x_i} + D_{qi} + \dot{q}_{sv} + \dot{q}_{sl} + \frac{1}{\rho_a} \frac{\partial (\rho_a V_s q_s)}{\partial z}. \quad (\text{A5})$$

The D terms represent diffusive/turbulent tendencies, R_θ is Rayleigh damping, V_l and V_s are fall velocities for liquid water and solid water (respectively), and ρ_a is dry-air density. The \dot{q} terms represent phase changes where the subscripts lv, sv, and sl represent, respectively, liquid-to-vapor, solid-to-vapor, and solid-to-liquid transfers (and vice versa). The L terms are the corresponding latent heats for these phase changes. We use the mass- and energy-conserving technique of Bryan and Fritsch (2002), for which

$$\begin{aligned} \Theta_1 &= \left(\frac{R_m}{c_{vm}} - \frac{R c_{pm}}{c_p c_{vm}} \right), \quad \Theta_2 = \frac{c_v}{c_{vm} c_p \pi}, \\ \Theta_3 &= -\theta \frac{R_v}{c_{vm}} \left(1 - \frac{R c_{pm}}{c_p R_m} \right), \\ \Pi_1 &= \frac{R c_{pm}}{c_p c_{vm}}, \quad \Pi_2 = \frac{R}{c_p} \left(\frac{1}{c_{vm} \theta} \right), \quad \Pi_3 = -\frac{R}{c_p} \left(\pi \frac{R_v c_{pm}}{R_m c_{vm}} \right), \\ \Pi_4 &= \frac{R \pi}{c_v \theta}, \quad \Pi_5 = \frac{R}{c_v \epsilon + q_v}, \end{aligned}$$

$$c_{pm} \equiv c_p + c_{pv} q_v + c_l q_l + c_s q_s,$$

$$c_{vm} \equiv c_v + c_{vv} q_v + c_l q_l + c_s q_s, \quad R_m \equiv R + R_v q_v,$$

where c_p and c_{pv} are the specific heats of dry air and water vapor (respectively) at constant pressure, c_v and c_{vv} are the specific heats of dry air and water vapor (respectively) at constant volume, c_l and c_s are the specific heats of liquid water and solid water (respectively), R and R_v are the gas constants for dry air and water vapor (respectively), and $\epsilon \equiv R/R_v$. Although not used herein, a traditional (nonconserving) equation set can be obtained by setting $c_{pv} = c_{vv} = c_l = c_s = R_v = \Pi_2 = \Pi_3 = \Pi_4 = \Pi_5 = 0$ in the equations above.

The definitions of π and θ are customary: $\pi \equiv (p/p_0)^{R/c_p}$ and $\theta \equiv T/\pi$, where p is pressure, $p_0 = 1000$ mb is a reference pressure, and T is temperature. Dry-air density ρ_a is obtained from the ideal gas law: $\rho_a = p_0 \pi^{c_v/R} (R_m \theta)^{-1}$. In all equations, prime superscripts indicate perturbations from a one-dimensional time-invariant hydrostatic reference profile.

The model is integrated using the split-explicit Runge–Kutta scheme for compressible equation sets following Wicker and Skamarock (2002). The simulations herein use a sixth-order flux-form advection scheme in the horizontal and a fifth-order scheme in the vertical. Explicit ∇^6 diffusion (Xue 2000) is applied in the horizontal to all variables except π . A positive-definite scheme is applied to the combination of advective and diffusive tendencies to ensure mass conservation. The subgrid turbulence scheme follows Deardorff (1980). Subgrid condensation/microphysics effects are not accounted for in these simulations.

For 2M simulations there are also equations for number concentration for every liquid/solid water component except for cloud liquid water. The numerical methods for advection and diffusion are the same as for mixing ratios.

b. Further details of the double-moment microphysics scheme

In the two-moment version of the scheme, N_0 and λ are free parameters that are determined from the predicted mixing ratio and number concentration for each species:

$$\lambda = \left[\frac{c N \Gamma(\mu + 4)}{q \Gamma(\mu + 1)} \right]^{1/d}, \quad (\text{A6})$$

$$N_0 = \left[\frac{N \lambda^{\mu+1}}{\Gamma(\mu + 1)} \right], \quad (\text{A7})$$

where Γ is the Euler gamma function and the parameters c and d are given by the assumed power-law mass–diameter (m – D) relationship of the hydrometeors for each species, where $m = c D^d$. Here, all particles are assumed to be spheres for simplicity, with a bulk particle density for the various ice species following Reisner et al.

(1998), except as described in section 2b for hail. Other details of the parameterization, including formulations for the various microphysical process rates, are given by Morrison et al. (2009) and references therein. For simplicity, we assume a constant cloud droplet concentration of 300 cm^{-3} . It is beyond the scope of this study to examine the impact of changes in droplet concentration due to different aerosol loadings; hence, this subject is left for future work.

c. Radar reflectivity

Radar reflectivity Z is calculated from integration of the size distributions for each species following Smith (1984). For simplicity, and since we are primarily interested in comparisons to widely available radar data, only Rayleigh scattering is considered whereas Mie scattering is ignored. This assumption is justified for the relatively large wavelength considered in this study (10 cm). For frozen species, a prefactor is used to compensate for the fact that the dielectric factor is with respect to water (not ice). The special case of partially melted snow and graupel utilizes the code of Blahak (2007) that allows for different ice lattice and water coating assumptions. This produces a radar bright band that appears physically reasonable and improves upon the assumption of no meltwater. The same reflectivity code and parameter settings (e.g., dielectric factor for ice) are used for all microphysical configurations, although the particle size distributions differ between 1M and 2M as described in section 2b.

REFERENCES

- Adlerman, E. J., and K. K. Droegemeier, 2002: The sensitivity of numerically simulated cyclic mesocyclogenesis to variations in model physical and computational parameters. *Mon. Wea. Rev.*, **130**, 2671–2691.
- Atlas, D., C. W. Ulbrich, F. D. Marks Jr., E. Amitai, and C. R. Williams, 1999: Systematic variation of drop size and radar-rainfall relations. *J. Geophys. Res.*, **104**, 6155–6169.
- Baldauf, M., A. Seifert, J. Förstner, D. Majewski, M. Raschendorfer, and T. Reinhardt, 2011: Operational convective-scale numerical weather prediction with the COSMO model: Description and sensitivities. *Mon. Wea. Rev.*, **139**, 3887–3905.
- Blahak, U., 2007: RADAR_MIE_LM and RADAR_MIELIB — Calculation of radar reflectivity from model output. Tech. Rep., Institute for Meteorology and Climate Research, University/Research Center Karlsruhe, 150 pp.
- Blyth, A. M., W. A. Cooper, and J. B. Jensen, 1988: A study of the source of entrained air in Montana cumuli. *J. Atmos. Sci.*, **45**, 3944–3964.
- Bryan, G. H., and J. M. Fritsch, 2002: A benchmark simulation for moist nonhydrostatic numerical models. *Mon. Wea. Rev.*, **130**, 2917–2928.
- , and M. D. Parker, 2010: Observations of a squall line and its near environment using high-frequency rawinsonde launches during VORTEX2. *Mon. Wea. Rev.*, **138**, 4076–4097.
- , J. C. Wyngaard, and J. M. Fritsch, 2003: Resolution requirements for the simulation of deep moist convection. *Mon. Wea. Rev.*, **131**, 2394–2416.
- , J. C. Knievel, and M. D. Parker, 2006: A multimodel assessment of RKW Theory's relevance to squall-line characteristics. *Mon. Wea. Rev.*, **134**, 2772–2792.
- Cohard, J.-M., and J.-P. Pinty, 2000: A comprehensive two-moment warm microphysical bulk scheme. I: Description and tests. *Quart. J. Roy. Meteor. Soc.*, **126**, 1815–1842.
- Cotton, W. R., G. H. Bryan, and S. C. van den Heever, 2011: *Storm and Cloud Dynamics*. 2nd ed. Academic Press, 809 pp.
- Dawson, D. T., M. Xue, J. A. Milbrandt, and M. K. Yau, 2010: Comparison of evaporation and cold pool development between single-moment and multimoment bulk microphysics schemes in idealized simulations of tornadic thunderstorms. *Mon. Wea. Rev.*, **138**, 1152–1171.
- Deardorff, J. W., 1980: Stratocumulus-capped mixed layer derived from a three-dimensional model. *Bound.-Layer Meteor.*, **18**, 495–527.
- Done, J., C. A. Davis, and M. Weisman, 2004: The next generation of NWP: Explicit forecasts of convection using the Weather Research and Forecasting (WRF) Model. *Atmos. Sci. Lett.*, **5**, 110–117.
- Dudhia, J., 1989: Numerical study of convection observed during the Winter Monsoon Experiment using a mesoscale two-dimensional model. *J. Atmos. Sci.*, **46**, 3077–3107.
- Ferrier, B. S., 1994: A double-moment multiple-phase four-class bulk ice scheme. Part I: Description. *J. Atmos. Sci.*, **51**, 249–280.
- , W.-K. Tao, and J. Simpson, 1995: A double-moment multiple-phase four-class bulk ice scheme. Part II: Simulations of convective storms in different large-scale environments and comparisons with other bulk parameterizations. *J. Atmos. Sci.*, **52**, 1001–1033.
- Fovell, R. G., and Y. Ogura, 1988: Numerical simulation of a mid-latitude squall line in two dimensions. *J. Atmos. Sci.*, **45**, 3846–3879.
- Ghan, S. J., L. R. Leung, and R. C. Easter, 1997: Prediction of cloud droplet number in a general circulation model. *J. Geophys. Res.*, **102**, 21 777–21 794.
- Gilmore, M. S., J. M. Straka, and E. N. Rasmussen, 2004a: Precipitation and evolution sensitivity in simulated deep convective storms: Comparisons between liquid-only and simple ice and liquid phase microphysics. *Mon. Wea. Rev.*, **132**, 1897–1916.
- , —, and —, 2004b: Precipitation uncertainty due to variations in precipitation particle parameters within a simple microphysics scheme. *Mon. Wea. Rev.*, **132**, 2610–2627.
- Grabowski, W. W., 1998: Toward cloud resolving modeling of large-scale tropical circulations: A simple cloud microphysics parameterization. *J. Atmos. Sci.*, **55**, 3283–3298.
- , 2001: Coupling cloud processes with the large-scale dynamics using the cloud-resolving convection parameterization (CRCP). *J. Atmos. Sci.*, **58**, 978–997.
- , and P. K. Smolarkiewicz, 1990: Monotone finite-difference approximations to the advection-condensation problem. *Mon. Wea. Rev.*, **118**, 2082–2097.
- , and H. Morrison, 2008: Toward the mitigation of spurious cloud-edge supersaturation in cloud models. *Mon. Wea. Rev.*, **136**, 1224–1234.
- , and Coauthors, 2006: Daytime convective development over land: A model intercomparison based on LBA observations. *Quart. J. Roy. Meteor. Soc.*, **132**, 317–344.

- Hong, S.-Y., J. Dudhia, and S.-H. Chen, 2004: A revised approach to ice microphysical processes for the bulk parameterization of clouds and precipitation. *Mon. Wea. Rev.*, **132**, 103–120.
- Houze, R. A., Jr., 1993: *Cloud Dynamics*. Academic Press, 573 pp.
- Kain, J. S., and Coauthors, 2008: Some practical considerations regarding horizontal resolution in the first generation of operational convection-allowing NWP. *Wea. Forecasting*, **23**, 931–952.
- Koenig, L. R., and F. W. Murray, 1976: Ice-bearing cumulus cloud evolution: Numerical simulation and general comparison against observations. *J. Appl. Meteor.*, **15**, 747–762.
- LaFore, J.-P., and M. W. Moncrieff, 1989: A numerical investigation of the organization and interaction of the convective and stratiform regions of tropical squall lines. *J. Atmos. Sci.*, **46**, 521–544.
- Lean, H. W., P. A. Clark, M. Dixon, N. M. Roberts, A. Fitch, R. Forbes, and C. Halliwell, 2008: Characteristics of high-resolution versions of the Met Office Unified Model for forecasting convection over the United Kingdom. *Mon. Wea. Rev.*, **136**, 3408–3424.
- Lin, Y.-L., R. D. Farley, and H. D. Orville, 1983: Bulk parameterization of the snow field in a cloud model. *J. Climate Appl. Meteor.*, **22**, 1065–1092.
- Liu, C., M. W. Moncrieff, and E. J. Zipser, 1997: Dynamical influence of microphysics in tropical squall lines: A numerical study. *Mon. Wea. Rev.*, **125**, 2193–2210.
- Locatelli, J. D., and P. V. Hobbs, 1974: Fallspeeds and masses of solid precipitation particles. *J. Geophys. Res.*, **79**, 2185–2197.
- Lord, S. J., H. E. Willoughby, and J. M. Piotrowicz, 1984: Role of parameterized ice-phase microphysics in an axisymmetric, nonhydrostatic tropical cyclone model. *J. Atmos. Sci.*, **41**, 2836–2848.
- Luo, Y., Y. Wang, H. Wang, Y. Zheng, and H. Morrison, 2010: Modeling convective-stratiform precipitation processes on a Mei-Yu front with the Weather Research and Forecasting model: Comparison with observations and sensitivity to cloud microphysics parameterizations. *J. Geophys. Res.*, **115**, D18117, doi:10.1029/2010JD013873.
- Martin, G. M., D. W. Johnson, and A. Spice, 1994: The measurement and parameterization of effective radius of droplets in warm stratocumulus clouds. *J. Atmos. Sci.*, **51**, 1823–1842.
- Matson, R. J., and A. W. Huggins, 1980: The direct measurement of the sizes, shapes and kinematics of falling hailstones. *J. Atmos. Sci.*, **37**, 1107–1125.
- McCumber, M., W.-K. Tao, J. Simpson, R. Penc, and S.-T. Soong, 1991: Comparison of ice-phase microphysical parameterization schemes using numerical simulations of tropical convection. *J. Appl. Meteor.*, **30**, 985–1004.
- Meyers, M. P., R. L. Walko, J. Y. Harrington, and W. R. Cotton, 1997: New RAMS cloud microphysics parameterization. Part II: The two-moment scheme. *Atmos. Res.*, **45**, 3–39.
- Milbrandt, J. A., and M. K. Yau, 2005a: A multimoment bulk microphysics parameterization. Part I: Analysis of the role of the spectral shape parameter. *J. Atmos. Sci.*, **62**, 3051–3064.
- , and —, 2005b: A multimoment bulk microphysics parameterization. Part II: A proposed three-moment closure and scheme description. *J. Atmos. Sci.*, **62**, 3065–3081.
- Ming, Y., V. Ramaswamy, L. J. Donner, V. T. Phillips, S. A. Klein, P. A. Ginoux, and L. W. Horowitz, 2007: Modeling the interactions between aerosols and liquid water clouds with a self-consistent cloud scheme in a general circulation model. *J. Atmos. Sci.*, **64**, 1189–1209.
- Morrison, H., and J. O. Pinto, 2005: Mesoscale modeling of springtime arctic mixed-phase stratiform clouds using a new two-moment bulk microphysics scheme. *J. Atmos. Sci.*, **62**, 3683–3704.
- , and —, 2006: Intercomparison of bulk cloud microphysics schemes in mesoscale simulations of springtime arctic mixed-phase stratiform clouds. *Mon. Wea. Rev.*, **134**, 1880–1900.
- , and W. W. Grabowski, 2008: A novel approach for representing ice microphysics in models: Description and tests using a kinematic framework. *J. Atmos. Sci.*, **65**, 1528–1548.
- , and J. Milbrandt, 2011: Comparison of two-moment bulk microphysics schemes in idealized supercell thunderstorm simulations. *Mon. Wea. Rev.*, **139**, 1103–1130.
- , J. A. Curry, and V. I. Khvorostyanov, 2005: A new double-moment microphysics parameterization for application in cloud and climate models. Part I: Description. *J. Atmos. Sci.*, **62**, 1665–1677.
- , J. O. Pinto, J. A. Curry, and G. M. McFarquhar, 2008: Sensitivity of modeled arctic mixed-phase stratocumulus to cloud condensation and ice nuclei over regionally varying surface conditions. *J. Geophys. Res.*, **113**, D05203, doi:10.1029/2007JD008729.
- , G. Thompson, and V. Tatarskii, 2009: Impact of cloud microphysics on the development of trailing stratiform precipitation in a simulated squall line: Comparison of one- and two-moment schemes. *Mon. Wea. Rev.*, **137**, 991–1007.
- Petch, J. C., and M. E. B. Gray, 2001: Sensitivity studies using a cloud-resolving model simulation of the tropical west Pacific. *Quart. J. Roy. Meteor. Soc.*, **127**, 2287–2306.
- , A. R. Brown, and M. E. B. Gray, 2002: The impact of horizontal resolution on the simulations of convective development over land. *Quart. J. Roy. Meteor. Soc.*, **128**, 2031–2044.
- Phillips, V. T., L. J. Donner, and S. T. Garner, 2007: Nucleation processes in deep convection simulated by a cloud-resolving model with double-moment bulk microphysics. *J. Atmos. Sci.*, **64**, 738–761.
- Pruppacher, H. R., and J. D. Klett, 1997: *Microphysics of Clouds and Precipitation*. Kluwer Academic Publishers, 954 pp.
- Randall, D., M. Khairoutdinov, A. Arakawa, and W. Grabowski, 2003: Breaking the cloud parameterization deadlock. *Bull. Amer. Meteor. Soc.*, **84**, 1547–1564.
- Redelsperger, J.-L., and Coauthors, 2000: A GCSS model intercomparison for a tropical squall line observed during TOGA-COARE. I: Cloud-resolving models. *Quart. J. Roy. Meteor. Soc.*, **126**, 823–863.
- Reisner, J., R. M. Rasmussen, and R. T. Bruintjes, 1998: Explicit forecasting of supercooled liquid water in winter storms using the MM5 mesoscale model. *Quart. J. Roy. Meteor. Soc.*, **124**, 1071–1107.
- Rotunno, R., Y. Chen, W. Wang, C. Davis, J. Dudhia, and G. J. Holland, 2009: Large-eddy simulation of an idealized tropical cyclone. *Bull. Amer. Meteor. Soc.*, **90**, 1783–1788.
- Rutledge, S. A., and P. V. Hobbs, 1984: The mesoscale and microscale structure and organization of clouds and precipitation in midlatitude cyclones. XII: A diagnostic modeling study of precipitation development in narrow cold-frontal rainbands. *J. Atmos. Sci.*, **41**, 2949–2972.
- Seifert, A., and K. D. Beheng, 2001: A double-moment parameterization for simulating autoconversion, accretion, and self-collection. *Atmos. Res.*, **59–60**, 265–281.
- , and —, 2006a: A two-moment cloud microphysics parameterization for mixed-phase clouds. Part 1: Model description. *Meteor. Atmos. Phys.*, **92**, 45–66.
- , and —, 2006b: A two-moment cloud microphysics parameterization for mixed-phase clouds. Part 2: Maritime vs.

- continental deep convective storms. *Meteor. Atmos. Phys.*, **92**, 67–82.
- Seity, Y., P. Brousseau, S. Malardel, G. Hello, P. Benard, F. Bouttier, C. Lac, and V. Masson, 2011: The AROME-France convective-scale operational model. *Mon. Wea. Rev.*, **139**, 976–991.
- Smith, P. L., 1984: Equivalent radar reflectivity factors for snow and ice particles. *J. Climate Appl. Meteor.*, **23**, 1258–1260.
- Stevens, B., R. L. Walko, W. R. Cotton, and G. Feingold, 1996: The spurious production of cloud-edge supersaturations by Eulerian models. *Mon. Wea. Rev.*, **124**, 1034–1041.
- Straka, J. M., and E. R. Mansell, 2005: A bulk microphysics parameterization with multiple ice precipitation categories. *J. Appl. Meteor.*, **44**, 445–466.
- Thompson, G., R. M. Rasmussen, and K. Manning, 2004: Explicit forecasts of winter precipitation using an improved bulk microphysics scheme. Part I: Description and sensitivity analysis. *Mon. Wea. Rev.*, **132**, 519–542.
- , P. R. Field, R. M. Rasmussen, and W. D. Hall, 2008: Explicit forecasts of winter precipitation using an improved bulk microphysics scheme. Part II: Implementation of a new snow parameterization. *Mon. Wea. Rev.*, **136**, 5095–5115.
- Tokay, A., and D. A. Short, 1996: Evidence from tropical raindrop spectra of the origin of rain from stratiform versus convective clouds. *J. Appl. Meteor.*, **35**, 355–371.
- Uijlenhoet, R., M. Steiner, and J. A. Smith, 2003: Variability of raindrop size distributions in a squall line and implications for radar rainfall estimation. *J. Hydrometeor.*, **4**, 43–61.
- VanWeverberg, K., N. vanLipzig, and L. Delobbe, 2010: Evaluation of moist processes during intense precipitation in km-scale NWP models using remote sensing and in-situ data: Impacts of microphysics size distribution assumptions. *Atmos. Res.*, **99**, 15–38.
- Waldvogel, A., 1974: The N_0 jump of raindrop spectra. *J. Atmos. Sci.*, **31**, 1067–1077.
- Weisman, M. L., J. B. Klemp, and R. Rotunno, 1988: Structure and evolution of numerically simulated squall lines. *J. Atmos. Sci.*, **45**, 1990–2013.
- , W. C. Skamarock, and J. B. Klemp, 1997: The resolution dependence of explicitly modeled convective systems. *Mon. Wea. Rev.*, **125**, 527–548.
- , C. Davis, W. Wang, K. W. Manning, and J. B. Klemp, 2008: Experiences with 0–36-h explicit convective forecasts with the WRF-ARW Model. *Wea. Forecasting*, **23**, 407–437.
- Weiss, S. J., M. E. Pyle, Z. Janjic, D. R. Bright, J. S. Kain, and G. J. DiMego, 2008: The operational High Resolution Window WRF model runs at NCEP: Advantages of multiple model runs for severe convective weather forecasting. Preprints, *24th Conf. on Severe Local Storms*, Savannah, GA, Amer. Meteor. Soc., P10.8. [Available online at <http://ams.confex.com/ams/pdfpapers/142192.pdf>.]
- Wicker, L. J., and W. C. Skamarock, 2002: Time splitting methods for elastic models using forward time schemes. *Mon. Wea. Rev.*, **130**, 2088–2097.
- Xu, K.-M., and Coauthors, 2002: An intercomparison of cloud-resolving models with the Atmospheric Radiation Measurement summer 1997 Intensive Observation Period data. *Quart. J. Roy. Meteor. Soc.*, **128**, 593–624.
- Xue, M., 2000: High-order monotonic numerical diffusion and smoothing. *Mon. Wea. Rev.*, **128**, 2853–2864.